The Astrophysical Journal, 692:422–442, 2009 February 10 doi:10.1088/0004-637X/692/1/422

MAMBO 1.2 mm OBSERVATIONS OF LUMINOUS STARBURSTS AT $z \sim 2$ IN THE SWIRE FIELDS

Carol J. Lonsdale[1,2], Maria del Carmen Polletta[2,3,4], Alain Omont[4], Dave Shupe[5], Stefano Berta[6,7], Robert Zylka[8], Brian Siana[5], Dieter Lutz[7], Duncan Farrah[9], Harding E. Smith[2,16], Guilaine Lagache[10], Carlos De Breuck[11], Frazer Owen[12], Alexandre Beelen[10], Dan Weedman[9], Alberto Franceschini[6], Dave Clements[13], Linda Tacconi[7], Alejandro Afonso-Luis[14], Ismael Pérez-Fournon[14], Pierre Cox[8], and Frank Bertoldi[15]

[1] Infrared Processing & Analysis Center, California Institute of Technology, 100-22, Pasadena, CA 91125, USA
[2] Center for Astrophysics & Space Sciences, University of California, San Diego, La Jolla, CA 92093-0424, USA
[3] INAF-IASF Milano, via E. Bassini, 20133, Italy; polletta@lambrate.inaf.it
[4] Institut d'Astrophysique de Paris, CNRS & Université Pierre et Marie Curie, 98bis, bd. Arago, 75014 Paris, France
[5] *Spitzer* Science Center, California Institute of Technology, 100-22, Pasadena, CA 91125, USA
[6] Dipartimento di Astronomia, Università di Padova, Vicolo dell'Osservatorio 3, 35122 Padova, Italy
[7] Max-Planck-Institut für extraterrestrische Physik, Postfach 1312, 85741 Garching, Germany
[8] Institute de Radioastronomie Millimetrique, 300 rue de la Piscine, 38406 St. Martin d'Heres, France
[9] Department of Astronomy, Cornell University, Ithaca, NY 14853, USA
[10] Institut d'Astrophysique Spatiale, Université de Paris XI, 91405 Orsay Cedex, France
[11] European Southern Observatory, Karl-Schwarzschild Strasse, 85748 Garching bei München, Germany
[12] National Radio Astronomy Observatory, P.O. Box O, Socorro, NM 87801, USA
[13] Astrophysics Group, Imperial College London, Prince Consort Road, London SW7 2AZ, UK
[14] Instituto de Astrofisica de Canarias, 38200 La Laguna, Tenerife, Spain
[15] Max-Planck-Institut für Radioastronomie, Auf dem Hügel 69, 53121 Bonn, Germany
Received 2007 December 10; accepted 2008 October 2; published 2009 February 19

ABSTRACT

We report on–off pointed MAMBO observations at 1.2 mm of 61 *Spitzer*-selected star-forming galaxies from the *Spitzer* Wide Area Infrared Extragalactic Legacy survey (SWIRE). The sources are selected on the basis of bright 24 μm fluxes ($f_{24\,\mu\mathrm{m}} > 0.4$ mJy) and of stellar dominated near-infrared spectral energy distributions in order to favor $z \sim 2$ starburst galaxies. The average 1.2 mm flux for the whole sample is 1.5 ± 0.2 mJy. Our analysis focuses on 29 sources in the Lockman Hole field where the average 1.2 mm flux (1.9 ± 0.3 mJy) is higher than in other fields (1.1 ± 0.2 mJy). The analysis of the multiwavelength spectral energy distributions indicates that these sources are starburst galaxies with far-infrared luminosities from 10^{12} to $10^{13.3}$ $L_\odot$, and stellar masses of $\sim$0.2–6 $\times$ 10^{11} $M_\odot$. Compared to submillimeter selected galaxies (SMGs), the SWIRE-MAMBO sources are among those with the largest 24 μm/1.2 mm flux ratios. The origin of such large ratios is investigated by comparing the average mid-infrared spectra and the stacked far-infrared spectral energy distributions of the SWIRE-MAMBO sources and of SMGs. The mid-infrared spectra, available for a handful of sources, exhibit strong polycyclic aromatic hydrocarbon (PAH) features, and a warm dust continuum. The warm dust continuum contributes $\sim$34% of the mid-infrared emission, and is likely associated with an AGN component. This contribution is consistent with what is found in SMGs. The large 24 μm/1.2 mm flux ratios are thus not due to AGN emission, but rather to enhanced PAH emission compared to SMGs. The analysis of the stacked far-infrared fluxes yields warmer dust temperatures than typically observed in SMGs. Our selection favors warm ultraluminous infrared sources at high-z, a class of objects that is rarely found in SMG samples. Indeed SMGs are not common among bright 24 μm sources (e.g., only about 20% of SMGs have $f_{24\,\mu\mathrm{m}} > 0.4$ mJy). Our sample is the largest *Spitzer*-selected sample detected at millimeter wavelengths currently available.

Key words: cosmology: observations – galaxies: formation – galaxies: high-redshift – galaxies: starburst – infrared: galaxies – submillimeter

Online-only material: color figures, extended figure

1. INTRODUCTION

After the discovery by *IRAS* of local Ultraluminous InfraRed Galaxies (ULIRGs, with $L_{\mathrm{FIR}} \gtrsim 10^{12}\ L_\odot$) and follow-up studies (see reviews by Sanders & Mirabel 1996; Lonsdale et al. 2006), the advent of sensitive submillimeter bolometer arrays heralded a revolution in our understanding of star formation at high redshift. Extragalactic surveys with SCUBA/JCMT (Hughes et al. 1998; Scott et al. 2002; Mortier et al. 2005; Coppin et al. 2006) and the Max Planck Millimeter Bolometer (MAMBO) array (Kreysa et al. 1998) at the Institut de Radioastronomie Millimétrique (IRAM) 30m telescope (Greve et al. 2004; Voss et al. 2006) show that the number of dusty, infrared-luminous galaxies (high-z ULIRGs, commonly "Submillimeter Galaxies" or SMGs) at $2 \lesssim z \lesssim 3$ is several orders of magnitude higher than in the local universe and that these distant SMGs contribute significantly to the universal star formation history (see e.g., Smail et al. 2004). SMGs appear to be "maximal starbursts" that form stars at the maximum global rate until a significant fraction of their original large gas mass is converted into a massive stellar system. Numerous follow-up studies indicate that SMGs are the most likely objects to trace the major episodes of star formation leading to the production of massive ($> 2L^*$) ellipticals (Greve et al. 2005; Tacconi et al. 2006). This picture is consistent with the claim that evolved massive ellipticals have formed the bulk of their stars in short (< 2 Gyr), intense bursts (Dunlop et al. 1996; Blakeslee et al. 1999). The evolution of SMGs into massive elliptical galaxies is often attributed to a negative feedback

[16] Deceased 2007 August 16.

mechanism induced by Active Galactic Nuclei (AGN) activity (Sanders et al. 1988). It is speculated that as the super-massive black hole (SMBH) in these systems reaches a certain mass and luminosity, the AGN will heat the surrounding gas, and thus halt any further star-forming activity and SMBH growth. This scenario is supported by deep X-ray observations of SMGs that show that some SMGs contain fast growing SMBHs (Alexander et al. 2005a; Borys et al. 2005).

In this context, identifying a large sample of ULIRGs at the epoch when these processes were taking place, i.e., $z \gtrsim 2$, is particularly important to understand the formation of the most massive galaxies, investigate the contribution of SMGs to the star formation history of the universe, and the presence and role of AGN activity. These goals have up to now been stymied by the limitations in mapping speed and sensitivity of the current submillimeter bolometers. The total number of known SMGs from all blank-field surveys with any instrument is less than five hundred. Their number and luminosity function are known from MAMBO/SCUBA counts, but remain uncertain at both low and high luminosities. Moreover, in order to quantify the relative importance of BH growth, stellar mass assembly, and the negative feedback induced into the host galaxies by these processes, it is necessary to separate any starburst and AGN power in these systems. Such an analysis requires multiwavelength coverage and good characterization of the spectral energy distributions (SEDs) and spectra. For these reasons, numerous efforts are being carried out to collect large samples of ULIRGs at $z \simeq 2$ with well sampled SEDs and spectra.

2. *SPITZER* OBSERVATIONS OF SUBMILLIMETER GALAXIES

With the advent of wide area *Spitzer* surveys, new breakthroughs in the study of SMGs are now possible as the statistics of the high redshift ULIRG population increase and the power sources in SMGs are quantified. In particular, the *Spitzer* Wide Area Infrared Extragalactic Survey (SWIRE[17]; Lonsdale et al. 2003), the largest ($\sim$50 deg^2) of the *Spitzer* suite of extragalactic surveys, with its sensitivity is able to detect many sources found in blank-field submillimeter/millimeter surveys. The SWIRE 5σ limits are 4.2, 7.5, 46, 47 μJy in the 4 IRAC (Fazio et al. 2004) bands at 3.6, 4.5, 5.8, and 8.0 μm, respectively, and 0.21, 30, and 180 mJy in the 3 MIPS (Rieke et al. 2004) bands at 24, 70, and 160 μm (Surace et al. 2005)[18]. Many previously known SMGs lie in the SWIRE fields and a large fraction of them are detected in 2 or more IR bands (see statistics below and Clements et al. 2008).

In order to estimate what fraction of SMGs would be detected by *Spitzer* to the SWIRE sensitivities, we gathered from the literature a sample of 90 SMGs with published *Spitzer* data, or that lie in the SWIRE fields (Greve et al. 2004; Ivison et al. 2004; Egami et al. 2004; Frayer et al. 2004a, 2004b; Chapman et al. 2004; Borys et al. 2005; Pope et al. 2006). This sample is not meant to be complete or exhaustive, but it includes a large number of objects that are representative of submillimeter selected SMGs ('classical SMGs' hereafter).

From an analysis of the SMGs with $f_{1.2\,\mathrm{mm}} > 2.5$ mJy or $S_{850\,\mu\mathrm{m}} > 7$ mJy (22 'bright SMGs'), we expect the large majority to be detected in at least 2 SWIRE bands. Ten (45%) of these 22 'bright SMGs' are detected above the SWIRE 24 μm $\sim 5\sigma$–6σ flux density limit ($\sim$250 μJy), 7 of them (32%) are brighter than 400 μJy, 20 (91%) are detected at both 3.6 and 4.5 μm above the SWIRE 5σ limits, 18% are detected at 5.8 μm and 27% at 8.0 μm[19].

The density of bright ($f_{1.2\,\mathrm{mm}} > 2.5$ mJy or $S_{850\,\mu\mathrm{m}} > 7$ mJy) SMGs is $\sim$230 per sq. deg. (Voss et al. 2006; Coppin et al. 2006), which means that in $\sim$50 sq. deg. SWIRE would detect with IRAC about $\sim$10,000 sources that are typical of those found in submillimeter surveys, and $\sim$5,000 at 24 μm (>3,000 brighter than 400 μJy), which is 10 times larger than all existing MAMBO-SCUBA surveys put together. Appreciable SWIRE detectability rates are also found for the submillimeter fainter SMGs ($3.2 < S_{850\,\mu\mathrm{m}} < 7$ mJy): 36% detectable at 24 μm (14% brighter than 400 μJy); 86% at 3.6 and 4.5 μm, 5% at 5.8 μm and 9% at 8 μm, so many thousand more submillimeter fainter SMGs are also to be found among SWIRE sources, including many 24 μm-detected sources. Moreover, *Spitzer* offers the opportunity to investigate possible selection biases inherent to submillimeter surveys in favor of objects dominated by cool dust.

The identification of high-z ULIRGs among the large SWIRE population of galaxies is not trivial, however, because they are faint in the optical and their optical–mid-IR SEDs can be similar to those of more quiescent star forming galaxies. Moreover, only long wavelength data (far-IR and mm/submillimeter) and reliable redshifts can confirm the extreme luminosities of the ULIRG candidates, but only 0.4% of the SWIRE population is detected at $\lambda \geqslant 70$ μm, and most of these ULIRG candidates are at $z < 1$ or too faint in the optical to be followed-up spectroscopically.

X-ray, radio, IR and CO studies (Alexander et al. 2005a; Chapman et al. 2005; Greve et al. 2005; Valiante et al. 2007; Menéndez-Delmestre et al. 2007) indicate that the far-IR (FIR) emission of the bulk of SMGs is dominated by starbursts, but a large fraction of them also host weak AGNs. *Spitzer* holds a key to this question because the diagnostic provided by the MIR broadband SEDs and IRS (Houck et al. 2004) spectra can discriminate warm AGN-dominated emission. Indeed, using IRS spectra, Pope et al. (2008) constrain the AGN contribution to the MIR emission of SMGs to <30%. However, *Spitzer* alone cannot determine the FIR luminosity or dust temperature of these systems because most of them are not detected at 70 and 160 μm.

Therefore, millimeter or submillimeter observations are needed to identify these objects and directly measure the long wavelength emission and estimate their FIR luminosities. The combination of SWIRE and MAMBO offers the possibility to explore the role of ULIRGs at $z \sim 2$ and determine their power sources.

We have thus undertaken a systematic observing program with MAMBO at 1.2 mm to search for luminous ULIRGs among SWIRE sources. The results from the first set of observations from this program are presented here.

This work is organized as follows. Section 3 describes the selection of the best candidates from the four northern SWIRE fields. Their observations with MAMBO are presented in Section 4. The spectral energy distributions (SEDs) of all sources and photometric redshift estimates are presented in Section 5. Millimeter and 24 μm fluxes, broadband SEDs,

[17] http://swire.ipac.caltech.edu/swire/swire.html

[18] The given SWIRE 5σ limits are valid for the LH field. They can differ by up to a factor of 1.2 in the other fields.

[19] The *Spitzer* 70 and 160 μm imaging sensitivity is such that extremely few high redshift ULIRGs are detectable in large area surveys such as SWIRE.

and colors of the selected sources are compared with those of submillimeter selected galaxies in Section 6. FIR luminosities and star formation rates (SFRs) are estimated by fitting greybody models with dust temperatures typically measured in SMGs, and presented in Section 7. Since the majority of the sources are not detected with MIPS at 70 and 160 μm, we measure average values from stacked MIPS images. The stacked FIR fluxes at 70 and 160 μm, combined with the average 24 μm and 1.2 mm fluxes, are used to characterize the FIR emission of these sources, and to compare it with the FIR emission of SMGs in Section 7. Stellar masses, near-IR (NIR) luminosities and star formation timescales are discussed in Section 8. The presence of AGN activity is investigated using different tracers, MIR spectra, X-ray, and radio observations in Section 9. The possible nature of the selected sources and their relation with classical SMGs are discussed in Section 10. Finally, our results are summarized in Section 11. Most of the analysis described here is applied to the subsample of sources from the Lockman Hole field. We only report the observations and resulting data on the sub-samples from the other fields. This choice is due to the fact that the Lockman Hole sub-sample is larger and better observed than those in the other fields. The sub-samples from the other fields do not allow us to carry out an accurate statistical analysis. We adopt a flat cosmology with $H_0 = 71$ km s^{-1} Mpc^{-1}, $\Omega_M = 0.27$ and $\Omega_\Lambda = 0.73$ (Spergel et al. 2003).

3. SAMPLE SELECTION

The most sensitive of the *Spitzer* MIPS bands for identification of distant ULIRGs is the 24 μm band. Therefore, we have searched for extreme ULIRGs among SWIRE sources with $f_{24} > 250$ μJy, corresponding to $\gtrsim 5\sigma$. Most systems above this f_{24} limit and $z > 1$ are expected to be ULIRGs. In addition distant ULIRGs will be faint at optical wavelengths, therefore we limited our overall $z > 1$ ULIRG samples to sources with $r' > 23$. This is a brighter cut than adopted in previous works targeting extreme 24 μm sources (e.g., Houck et al. 2005; Yan et al. 2005). For our purpose, we prefer to adopt a brighter optical limit because a fainter cut can reject ULIRGs with colors like some local well known examples, e.g., an Arp 220-like system ($z = 0.018$ and L(IR) $= 1.45 \times 10^{12}$ $L_\odot$) at $z = 1$ with an observed $f_{24} = 250$ μJy would have a luminosity of $L_{\rm IR} = 10^{12.6}$ $L_\odot$ and an observed magnitude $r' = 23.4$, while an Arp 220-like system with $L_{\rm IR} = 10^{13}$ $L_\odot$ at $z = 1$ would have an observed $r' = 22.4$.

The selection based on bright 24 μm and faint r'-band fluxes yields consequently sources with large $f_{24\,\mu{\rm m}}/f_r$ ratios, typically $\gtrsim$100. Bright 24 μm *Spitzer* samples with large IR/optical flux ratios (i.e., $f_{24\,\mu{\rm m}}/f_R > 500$) tend to be dominated by AGN light in the MIR (Houck et al. 2005; Yan et al. 2005; Sajina et al. 2007; Brand et al. 2006; Dey et al. 2008). Moreover MAMBO observations of these have shown that they are weak at 1.2 mm compared to submillimeter selected SMGs (Lutz et al. 2005). An additional selection criterion was thus applied to disfavor AGN-dominated and favor star-forming-dominated systems. The additional selection criterion is based on the evidence in the IRAC bands for the ~ 1.6 μm rest-frame Planck spectrum peak from evolved stars. Note that IRAC was in part designed for photometric selection of galaxies at $z = 1.5$–3 displaying this feature (Simpson & Eisenhardt 1999; Sawicki 2002). Such a peak is not observed in templates of local AGN-dominated sources such as Mrk 231, IRAS 19254−7245 (Berta et al. 2003), or in type 1 QSOs (Elvis et al. 1994). On the other hand, the SED of sources displaying such a peak can be well fitted by local star formation-dominated templates, such as M 82, and Arp 220 (Silva et al. 1998).

Furthermore, we have selected sources where this peak lies in the 5.8 μm band in order to favor sources at $z = 1.5$–3. We refer to such sources as '5.8 μm-peaker' (or 'b3' for bump in the third IRAC channel). Formally a source is defined '5.8 μm-peaker' if satisfies the following condition: $f_{3.6} < f_{4.5} < f_{5.8} > f_{8.0}$ where f is the flux density in μJy and $f_{8.0}$ can also be an upper limit (typically at 5σ).

We have previously demonstrated that this selection method is effective in finding starburst-dominated objects at $z = 1.5$–3 (Weedman et al. 2006; Berta et al. 2007b; Farrah et al. 2008). IRS MIR spectroscopic observations of a similar sample of 32 SWIRE sources displaying a rest-frame NIR bump peaking at 4.5 μm demonstrate that they are star-forming dominated (Farrah et al. 2008). Most of their spectra exhibit prominent PAH emission features consistent with a starburst origin of their MIR emission. Similarly, Weedman et al. (2006) find that all SWIRE sources with a NIR bump at 5.8 μm, display PAH emission features in their IRS spectra. Moreover, eight of the sources selected here were observed in the MIR by the IRS instrument on *Spitzer* (six in the LH Weedman et al. 2006, and two in the EN2 field, C. J. Lonsdale 2009, in preparation), and their spectra display strong PAH features as expected from starburst-dominated emission. The IRS observations yield spectroscopic redshifts that, in all but one case, confirm the '5.8 μm-peakers' photometric redshift selection method. The agreement between photometric and IRS redshifts is discussed further in Section 5 (see also Farrah et al. 2008). Based on these considerations and studies, we infer that the combination of a strong 24 μm flux and a peak in the IRAC bands is a good indication of the presence of PAH emission at $z \sim 2$, and thus of a significant, and likely dominant, starburst contribution to the NIR and MIR emission. Although in some cases an AGN component in the MIR can be present, its contribution is never dominant compared to the starburst component (Berta et al. 2007a).

In order to further increase the chance of selecting $z \sim 2$ star-forming galaxies, we derived photometric redshifts for all source candidates (for a detailed description of the procedure see Section 5).

We have selected in this manner 1023 '5.8 μm-peaker' ULIRG candidates with $f_{24} > 250$ μJy, $r' > 23$, and photometric redshift in the range 1.5–3, from the SWIRE's largest field (11 deg^2), the Lockman Hole (LH). We restricted the search to the region in the LH with available optical imaging ($\sim$9.5 deg^2). At similar redshifts and for fixed SED shape the most luminous objects will be the brightest in flux. Therefore, to cull from this large sample the most luminous candidates we selected the brightest 24 μm sources, i.e., $f_{24} > 400$ μJy, among all '5.8 μm-peakers', and with $\geqslant 5\sigma$ detections in the first 3 IRAC bands. There are 520 sources with $f_{24} > 400$ μJy, corresponding to 55 sources per square degree. We have also required unambiguous (unique or not detected counterpart) source identification at all optical-MIPS wavelengths in the images, so that source confusion would not affect the SED interpretation. Our selection is likely to strongly favor sources with strong 7.7 μm PAH features in 24 μm band in the $z = 2$ range.

Finally we made estimates of the expected 1.2 mm flux densities by fitting templates of various local starbursts and ULIRGs to the optical ($Ugriz$) and infrared (3.6–24 μm) bands. Since most of the candidates are not detected at 70 or 160 μm,

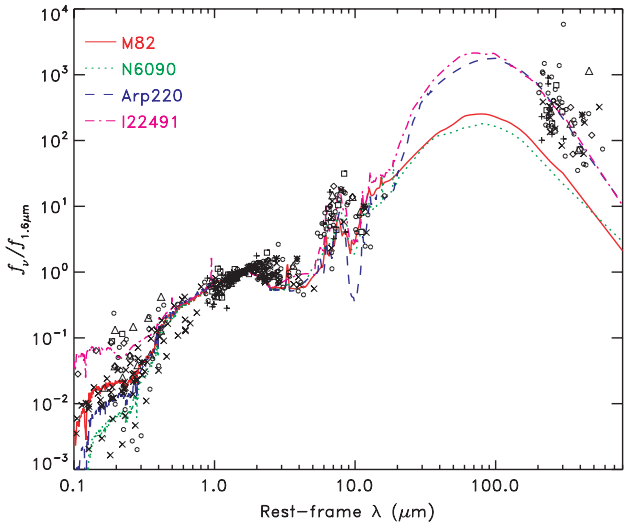

Figure 1. Rest-frame SEDs normalized at 1.6 μm of submillimeter selected galaxies from the literature (open circles: HDFN sources from Pope et al. (2006); crosses: GOODS sources from Borys et al. (2005); squares: Lockman Hole sources, and triangles: ELAIS-N2 sources from Chapman et al. (2004); diamonds: Lockman Hole sources from Greve et al. (2004); stars: FLS sources from Frayer et al. (2004a); and plus signs: GOODS sources from Egami et al. (2004). The curves represent various starburst galaxy templates: M 82 (solid red), NGC 6090 (dotted green), Arp 220 (dashed blue), and I22491 (dot-dashed magenta).

their FIR through mm spectral shape is unconstrained. The MAMBO flux predictions therefore rest on the adoption of a long wavelength SED template. To select appropriate templates we build the rest-frame SEDs of ∼30 SMGs with known redshifts and available IRAC and 24 μm fluxes, and normalized them at rest-frame 1.6 μm. We then selected templates of local starburst-dominated ULIRGs which pass approximately through the midst of the distribution of 850 μm and 1.2 mm points for these objects, as shown in Figure 1. Most of the SMGs have FIR SEDs similar to Arp 220 or IRAS 22491−1808 (I22491 hereafter). The main difference between the Arp 220 and I22491 templates, a starburst dominated and a composite starburst+AGN system, respectively, resides at optical and MIR wavelengths. However, since with some extinction the optical emission of I22491 resembles that of Arp 220, and in the MIR we do not have enough spectral coverage to favor one template with respect to the other, we decided to fit each candidate source with an Arp 220 template. In addition we decided to also fit a template with a much lower FIR/NIR flux ratio than Arp 220, to obtain minimum estimates of the predicted 1.2 mm flux for each source. For this we chose NGC 6090, a local starburst with a similar SED shape to the well known starburst galaxy M 82. Examples of these two fits are shown for 3 sources in Figure 2, where it can be seen that the two templates produce similar photometric redshifts from the IRAC data, but the predictions for the bolometric luminosity, and for the 1.2 mm flux density differ by a factor of about 10.

To select the best candidates for observations with MAMBO, we averaged the predicted 1.2 mm flux density for each source from both templates and ordered the sources according to decreasing predicted averaged 1.2 mm flux. While this procedure may not predict the 1.2 mm flux of an individual source accurately, because the actual long wavelength SED is unconstrained, it does provide a robust way to prioritize them by decreasing the expected 1.2 mm flux under the assumption that they have similar SED shapes, and taking into account the sources redshift.

The same selection procedure was applied to other three SWIRE fields, *XMM*-LSS (*XMM*), ELAIS-N1 (EN1) & ELAIS-N2 (EN2). A description of the fields sizes and multiwavelength coverage can be found in Surace et al. (2005). The top 61 sources from the 4 SWIRE fields, (LH, *XMM*, EN1 & EN2), were observed with MAMBO at 1.2 mm. The largest number of sources was selected in the LH field, 29 sources, compared to 17 in EN1, 9 in EN2, and 6 in *XMM*. The 29 LH sources correspond to 5.6% of the entire sample of 520 $f_{24} > 400$ μJy '5.8 μm peakers'. The predicted 1.2 mm fluxes (averaged on all templates) range from 1.4 to 25 mJy. The list of selected sources, coordinates and optical–infrared–mm fluxes are reported in Tables 1 and 2.

Note that because of the uncertainties on the IRAC fluxes, especially at 5.8 and 8.0 μm, which are less sensitive bands than those at shorter wavelengths, a '5.8 μm-peaker' ($z \sim 2.2$–3.2) can become '4.5 μm' or '8.0 μm-peakers' ('b2', or 'b4') in different versions of the data processing. Indeed, some of the sources selected here, that were classified '5.8 μm-peakers' based on a previous version of the SWIRE catalog used during the selection process, show a peak at shorter ('b2'; $z \sim 1.5$–2.2) or longer wavelengths ('b4'; $z \geqslant 3.2$) or a flat IRAC SED ('fl') in the latter SWIRE catalogs that is used in this work. This change is observed in 14 out of 61 selected objects (see last column of Table 1).

4. MAMBO OBSERVATIONS AND RESULTS

Observations were spread over the pool observing sessions at the IRAM 30m telescope in fall/winter 2005/2006, using the 117 element version of the MAMBO array (Kreysa et al. 1998) operating at a wavelength of 1.2 mm (250 GHz). On the first run in late October - early November 2005 we observed most of the Lockman sample (29 sources), and the 6 *XMM* sources. During the winter run, mainly early March 2006, the observations of the Lockman sample were completed and exploratory observations of the 17 EN1 and 9 EN2 sources were carried out.

We used the standard on-off photometry observing mode, chopping between the target and sky at 2 Hz, and nodding the telescope every 10 or 20 s. On-off observations were typically obtained in blocks of six scans of 16 or 20 10 s subscans each, and repeated in later observing nights. The atmospheric transmission was intermediate with $\tau(1.2\,\mathrm{mm})$ at zenith between 0.1 and 0.4. The absolute flux calibration was established by observations of Mars and Uranus, resulting in a flux calibration uncertainty of about 20%.

On average, the noise of the channel used for point-source observations was about 35–40 mJy/$\sqrt{t}$/beam, where t is the exposure time in seconds, consistent with the MAMBO time estimator for winter conditions. In order to identify a maximum number of strong sources with flux density ∼3–5 mJy within the allocated time (57 hr, i.e., ∼38 hr of integration time), we adopted a two-step procedure: a first exploratory phase generally aiming at an rms ∼1.0–1.2 mJy; then longer integrations on sources showing hints of detection in order to reach rms ≈ 0.6–0.7 mJy and achieve 3–5σ detections of sources stronger than ∼2–3 mJy. However, we were able to apply such a complete procedure only to the LH sample (29 sources), which had the best selection and was the only one observable in good conditions (during night or early morning) both in fall and winter runs. The observations of the sources of the three other fields (EN1 and EN2, *XMM*; 32 sources) were more or less limited to the exploratory phase.

Table 1
Basic Properties of the SWIRE-MAMBO Sample

Source ID	IAU Name[a]	α_{2000} (degrees)	δ_{2000} (degrees)	z	$f_{1.2\,mm}$ (mJy)	f_{70} (mJy)	f_{160} (mJy)	$f_{20\,cm}$ (mJy)	Notes[b]
				Lockman-Hole					
				5σ					
LH-01	SJ105007.26+571651.0	162.53026	57.280842	1.35	5.65 ± 0.74	<18	<108	···	b3
LH-02	SJ103639.57+575346.6	159.16486	57.896271	1.93	5.29 ± 0.85	<18	<108	···	b3
LH-03	SJ104313.33+574621.0	160.80553	57.772511	2.67	3.79 ± 0.76	<18	<108	···	b3
				4σ					
LH-04	SJ104208.52+582433.3	160.53551	58.409241	2.94	2.80 ± 0.57	<18	<108	···	b3
LH-05	SJ103744.45+582950.7	159.43521	58.497410	1.88[c]	2.93 ± 0.61	<18	<108	···	b3/IRS(B5)
LH-06	SJ103837.03+582214.7	159.65428	58.370762	1.68[c]	3.83 ± 0.84	<18	<108	···	b2/IRS(B4)
LH-07	SJ105405.50+581400.1	163.52290	58.233349	1.82[c]	2.76 ± 0.60	<18	<108	···	b3/IRS(B3)
				3σ					
LH-08	SJ104616.97+580451.9	161.57072	58.081081	2.01	2.52 ± 0.74	<18	<108	···	b3
LH-09	SJ104616.96+581659.3	161.57066	58.283150	2.28	1.76 ± 0.56	<18	<108	···	b3
				2σ					
LH-10	SJ103450.43+574116.0	158.71011	57.687771	2.23	2.29 ± 0.77	<18	<108	···	b3/X[d]
LH-11	SJ104601.78+590916.9	161.50743	59.154690	1.66	2.06 ± 0.79	<18	<108	0.082 ± 0.004	b3
LH-12	SJ104839.33+592149.0	162.16386	59.363609	1.89[c]	2.56 ± 1.08	<18	<108	···	b4/IRS(B8)
				1σ					
LH-13	SJ104656.24+594008.0	161.73434	59.668900	1.70	1.92 ± 0.98	<18	<108	···	b2
LH-14	SJ104724.25+572150.6	161.85106	57.364052	2.03	1.95 ± 1.03	<18	<108	···	b3
LH-15	SJ104822.05+583828.2	162.09186	58.641171	2.80	1.13 ± 0.77	<18	<108	···	b4
LH-16	SJ103809.63+591650.1	159.54013	59.280590	2.40	1.57 ± 1.08	<18	<108	···	b4
LH-17	SJ105750.75+571652.7	164.46147	57.281300	1.85	1.47 ± 1.10	<18	<108	···	b3
LH-18	SJ105943.13+580849.1	164.92970	58.146969	2.16	1.46 ± 1.09	<18	<108	···	b3
LH-19	SJ104716.02+593201.3	161.81674	59.533691	2.11	1.87 ± 1.58	<18	<108	···	b2/X
LH-20	SJ104816.14+592943.3	162.06725	59.495350	1.90	1.04 ± 1.00	<18	<108	···	b2
				$<1\sigma$					
LH-21	SJ103704.32+584755.1	159.26801	58.798641	2.63	0.75 ± 0.90	<18	<108	···	b3
LH-22	SJ104646.02+590517.5	161.69173	59.088188	1.54	1.40 ± 1.78	<18	<108	0.051 ± 0.004	b2
LH-23	SJ103809.17+583226.1	159.53822	58.540581	0.98[c]	0.93 ± 1.17	<18	<108	···	b3/IRS(B6)
LH-24	SJ103647.44+591819.5	159.19765	59.305408	1.25	1.19 ± 1.57	<18	<108	···	b3
LH-25	SJ104059.86+574536.7	160.24942	57.760201	2.13	0.74 ± 1.06	<18	<108	···	b3
LH-26	SJ103856.94+585244.0	159.73723	58.878891	1.88[c]	0.44 ± 0.93	<18	<108	···	b3/IRS(B7)
LH-27	SJ104553.76+565930.9	161.47398	56.991909	2.01	−0.10 ± 1.45	<18	<108	···	b3
LH-28	SJ104942.11+561234.5	162.42545	56.209579	2.82	−0.14 ± 1.31	19 ± 1	<108	2.73 ± 0.14	b4/X
LH-29	SJ103500.98+573847.5	158.75407	57.646519	2.16	−1.49 ± 1.18	<18	<108	···	b3
				ELAIS-N1					
				3σ					
EN1-01	SJ160343.08+551735.8	240.92949	55.293282	2.37	2.81 ± 0.78	<17	<104	···	b3
EN1-02	SJ160440.45+543103.0	241.16856	54.517490	1.93	2.46 ± 0.81	<17	<104	···	b3
EN1-03	SJ160651.22+545338.0	241.71341	54.893879	1.90	2.11 ± 0.69	<17	<104	···	b3
				2σ					
EN1-04	SJ161658.14+535319.3	244.24226	53.888691	2.00	2.82 ± 0.99	<17	81 ± 4	···	b3
EN1-05	SJ161412.14+541927.2	243.55058	54.324211	1.88	2.09 ± 1.03	<17	<104	···	b3
				1σ					
EN1-06	SJ160502.00+540639.0	241.25833	54.110840	2.37	1.15 ± 0.86	<17	<104	···	b3
EN1-07	SJ160409.72+541808.9	241.04051	54.302460	1.40	1.25 ± 1.01	<17	<104	···	b3
EN1-08	SJ162002.45+542933.8	245.01019	54.492710	2.03	1.26 ± 1.02	<17	<104	···	b3
				$<1\sigma$					
EN1-09	SJ161950.53+553740.9	244.96054	55.628040	1.69	1.07 ± 1.73	<17	<104	···	b2
EN1-10	SJ160945.58+534757.9	242.43991	53.799412	2.38	0.74 ± 1.23	<17	<104	···	b4
EN1-11	SJ161632.58+540736.9	244.13573	54.126919	1.55	0.56 ± 1.04	<17	<104	···	b3
EN1-12	SJ161358.92+542812.2	243.49551	54.470051	2.11	0.04 ± 1.81	<17	55 ± 4	···	b3
EN1-13	SJ155904.74+551137.2	239.76977	55.193661	1.95	−0.11 ± 1.37	<17	<104	···	b3
EN1-14	SJ161753.53+541840.9	244.47304	54.311352	2.39	−0.27 ± 2.00	<17	<104	···	b3
EN1-15	SJ161642.78+542355.6	244.17825	54.398769	1.96	−0.46 ± 1.99	<17	<104	···	b3
EN1-16	SJ161414.48+554255.4	243.56035	55.715401	2.22	−0.99 ± 2.26	<17	<104	···	b3
EN1-17	SJ160611.83+551832.5	241.54930	55.309040	2.15	−0.61 ± 1.38	<17	<104	···	b3
				ELAIS-N2					
				3σ					
EN2-01	SJ163734.44+415151.4	249.393494	41.864269	1.85	2.52 ± 0.70	<18	<124	···	b3
				1σ					
EN2-02	SJ163528.58+403843.9	248.869080	40.645519	1.57	2.60 ± 1.47	11 ± 1	110 ± 4	···	b2

Table 1
(Continued)

Source ID	IAU Name[a]	α_{2000} (degrees)	δ_{2000}	z	$f_{1.2\,mm}$ (mJy)	f_{70}	f_{160} (mJy)	$f_{20\,cm}$	Notes[b]
EN2-03	SJ164058.63+415432.2	250.244308	41.908958	1.77[c]	1.15 ± 0.80	<18	<124	···	fl/IRS
EN2-04	SJ163022.17+404957.5	247.592380	40.832649	1.69[c]	1.17 ± 0.83	<18	<124	···	b4/IRS
					$<1\sigma$				
EN2-05	SJ163506.01+411735.1	248.775055	41.293072	2.06	1.10 ± 1.16	<18	<124	···	b3
EN2-06	SJ163748.16+404922.1	249.450653	40.822811	1.95	0.90 ± 1.21	<18	<124	···	b3
EN2-07	SJ163729.80+415722.1	249.374176	41.956150	2.15	0.35 ± 1.55	<18	<124	···	
EN2-08	SJ163424.64+410954.5	248.602676	41.165131	1.96	0.08 ± 1.07	<18	<124	···	b3
EN2-09	SJ163755.89+413416.8	249.482895	41.571320	2.18	-0.24 ± 2.02	<18	<124	···	b3
					XMM-LSS				
					4σ				
XMM-01	SJ021926.24-045212.9	34.85934	−4.870250	1.89	3.20 ± 0.71	<24	<126	···	b3
					3σ				
XMM-02	SJ022521.66-053545.7	36.34024	−5.596040	1.93	2.45 ± 0.61	<24	103 ± 4	···	b3
XMM-03	SJ021933.90-043335.5	34.89124	−4.559850	2.11	2.17 ± 0.71	<24	<126	···	b3/X
					1σ				
XMM-04	SJ021925.60-032317.4	34.85665	−3.388180	2.12	1.46 ± 0.80	<24	<126	···	b3
					$<1\sigma$				
XMM-05	SJ021947.11-060017.7	34.94630	−6.004930	1.01	0.78 ± 0.90	<24	<126	···	b3
XMM-06	SJ022512.20-053119.6	36.30082	−5.522100	1.01	0.90 ± 1.10	<24	<126	···	b2

Notes. The sources are ordered by field and signal-to-noise ratio at 1.2 mm.
[a] SJ stands for SWIRE J. SWIRE JHHMMSS.ss+DDMMSS.s is the official IAU source name for sources discovered in the SWIRE fields.
[b] Shape of the IRAC SED (b2: peak at 4.5 μm, b3: peak at 5.8 μm, b4: peak at 8.0 μm, fl: flat IRAC SED). Sources with IRS observations are marked with IRS. B# refers to the source ID in Weedman et al. (2006). Sources with X-ray coverage are marked with X.
[c] Spectroscopic z from IRS spectrum. IRS spectra of LH sources are published in Weedman et al. (2006), those of EN2 will be published in a future publication (C. J. Lonsdale et al. 2009, in preparation).
[d] X-ray source 425 in CLASX catalog (Yang et al. 2004), F(0.4–8 keV) = 2.1×10^{-15} erg cm^{-2} s^{-1} and HR = −0.7.

A major change occurred in the 30 m telescope control system in 2005. MAMBO pool observations in our October to early November session were carried out with a well known system which had been in use for years. A new system, just installed before the winter pool session, brought some problems such as stronger accelerations of the telescope during nodding with possible effects on tracking accuracy and temperature stability of the helium cryostat in some circumstances; anomalous noise in some MAMBO channels for a few cases; etc. These problems induced some delays and loss of time, but they were practically all well under control for most of our observations in 2006 February–March. The data were reduced with standard procedures in the MOPSIC package developed by R. Zylka. Great care was taken to check the quality of the data obtained with the new control system, and we discarded the data from about ten scans displaying obvious problems such as anomalous noise in some channels, as well as ∼3% of the data taken in periods when we are not sure that the problems with the new system were well under control.

Table 1 lists the resulting 1.2 mm flux densities and their statistical uncertainties. In the more completely studied Lockman sample (29 sources, Table 1), more than 40% of the sources (12) show a signal at $>2.5\sigma$, and fluxes $\gtrsim$2 mJy (corresponding to ∼5 mJy at 850 μm for $z \sim 2$, see Greve et al. 2004). Eight of them have 1.2 mm fluxes in the 3–5 mJy range, with signal-to-noise ratio (S/N) $\gtrsim$ 4–5, which guarantees the robustness of the detections. However, it is possible that the flux densities of the detected sources are slightly overestimated by the Malmquist bias, by an amount that probably does not exceed 10% on average. The average flux density of the 29 LH sources is 1.88 ± 0.28 mJy (see Table 3), corresponding to ∼5 mJy at 850 μm at $z \sim 2$).

As quoted, the remaining 32 sources, from EN1 & EN2 and *XMM*, were not observed as completely. However, the average strength of the sources in the other fields is significantly weaker (1.14 ± 0.20 mJy) than in the Lockman sample. The fraction of sources showing at least a 2.5σ signal is only 25% (8 sources), there is practically no source stronger than 3 mJy, and the average of the 23 other undetected sources is only 0.60 ± 0.17 mJy. Possible reasons for such a behavior are either a pointing problem caused by the system changes implemented in 2005, or a bias introduced by the slight different selection criteria (see Section 6.1).

Table 3 summarizes the information about the number of sources showing a signal at various levels and the average values for two sub-samples and the totality of the 61 sources.

5. PHOTOMETRIC REDSHIFTS AND SED FITS

In order to classify the spectral energy distributions (SEDs) and estimate photometric redshifts of the sources in the sample, optical and IR data ($\leqslant$24 μm) are combined and fitted with various galaxy templates. The SEDs are fitted using the Hyper−z code (Bolzonella et al. 2000). Hyper−z finds the best-fit by minimizing the χ^2 derived from the comparison of the observed SED and expected SEDs at various redshifts, and using a template library and the same photometric system. The effects of dust extinction are taken into account by reddening the reference templates according to a selected reddening law. We use the prescription for extinction measured in high-redshift starbursts by Calzetti et al. (2000). We limit the additional extinction A_V to be less than 2.0 mag and include templates of highly extinguished objects. We used two template libraries, one with 105 templates of starburst galaxies (Chary & Elbaz 2001), and one with 8 templates including 2 late-spirals, 5 starbursts, and 1 composite (starburst+AGN) template covering the wavelength range between 1000 Å and 1000 μm.

Table 2
Optical & Infrared Data of the SWIRE-MAMBO Sample

Source ID	u	g'	r' (Vega)	i'	z	$f_{3.6}$	$f_{4.5}$	$f_{5.8}$ (μJy)	$f_{8.0}$	f_{24}
LH-01	···	25.41	23.75	22.97	···	89	94	108	<47	755
LH-02	···	>25.2	>24.4	>23.5	···	41	62	72	<47	837
LH-03	···	24.82	24.54	23.61	···	39	52	78	64	721
LH-04	···	>25.2	24.06	>23.5	···	44	63	100	99	707
LH-05	···	24.40	23.45	22.73	···	77	93	98	78	1502
LH-06	···	25.50	>24.4	23.61	···	68	92	97	72	1072
LH-07	···	25.23	24.68	23.98	···	37	47	62	42	1203
LH-08	···	>25.2	>24.4	>23.5	···	65	84	116	61	515
LH-09	···	24.86	24.23	23.46	···	60	76	95	85	832
LH-10	···	26.39	25.84	24.77	···	28	45	65	<47	484
LH-11	>24.3	25.05	23.70	23.17	22.36	70	91	95	70	1034
LH-12	···	···	22.62	···	···	75	95	120	125	1419
LH-13	24.20	24.83	>24.4	>23.5	···	50	67	57	<47	755
LH-14	···	25.33	24.36	23.24	···	42	53	84	<47	795
LH-15	>24.3	>25.2	23.97	23.33	···	54	75	114	123	638
LH-16	···	>25.2	>24.4	···	···	36	46	62	81	1318
LH-17	···	···	24.88	23.81	···	81	102	104	68	982
LH-18	···	>25.2	>24.4	>23.5	···	20	28	59	<47	967
LH-19	>24.3	>25.2	>24.4	>23.5	···	33	40	57	<47	488
LH-20	>24.3	>25.2	>24.4	>23.5	···	35	44	48	<47	474
LH-21	···	>25.2	23.58	>23.5	···	54	77	103	104	733
LH-22	>24.3	>25.2	>24.4	>23.5	>23.6	31	40	38	36	446
LH-23	···	>25.2	>24.4	>23.5	···	26	33	40	<47	1111
LH-24	···	24.77	24.07	23.00	···	75	88	103	81	899
LH-25	···	>25.2	>24.4	>23.5	···	31	42	51	46	430
LH-26	···	>25.2	>24.4	>23.5	···	26	45	47	<47	1105
LH-27	···	>25.2	23.51	>23.5	···	43	54	64	<47	673
LH-28	···	···	23.65	···	···	30	40	46	53	499
LH-29	···	>25.2	>24.4	>23.5	···	31	39	58	<47	451
EN1-01	>23.4	>24.94	>24.04	>23.18	>21.9	35	48	63	59	698
EN1-02	>23.4	>24.94	>24.04	>23.18	>21.9	37	53	68	44	771
EN1-03	>23.4	>24.94	>24.04	>23.18	>21.9	41	52	57	46	823
EN1-04	>23.4	24.42	>24.04	>23.18	>21.9	39	49	77	37	657
EN1-05	>23.4	>24.94	>24.04	23.14	>21.9	30	40	53	<47	607
EN1-06	>23.4	>24.94	>24.04	>23.18	>21.9	27	37	<40	53	458
EN1-07	>23.4	>24.94	>24.04	>23.18	>21.9	54	67	62	<47	560
EN1-08	>23.4	>24.94	>24.04	>23.18	>21.9	19	32	44	34	628
EN1-09	>23.4	>24.94	>24.04	>23.18	>21.9	70	93	88	56	581
EN1-10	>23.4	>24.94	>24.04	>23.18	>21.9	24	37	56	51	446
EN1-11	>23.4	>24.94	>24.04	>23.18	>21.9	37	<8	51	67	673
EN1-12	>23.4	>24.94	>24.04	>23.18	>21.9	44	53	80	63	879
EN1-13	>23.4	>24.94	>24.04	>23.18	>21.9	35	44	51	46	694
EN1-14	>23.4	>24.94	>24.04	>23.18	>21.9	35	46	75	72	550
EN1-15	>23.4	>24.94	>24.04	>23.18	>21.9	33	42	55	<47	631
EN1-16	>23.4	>24.94	>24.04	>23.18	>21.9	28	35	48	<47	546
EN1-17	>23.4	>24.94	>24.04	>23.18	>21.9	26	41	65	43	599
EN2-01	>23.4	>24.94	>24.04	>23.18	>21.9	45	58	59	40	814
EN2-02	>23.4	>24.94	>24.04	>23.18	>21.9	36	53	48	58	928
EN2-03	>23.4	>24.94	>24.04	>23.18	>21.9	49	54	67	53	1237
EN2-04	>23.4	23.70	>24.04	>23.18	>21.9	83	115	129	173	1521
EN2-05	>23.4	>24.94	>24.04	>23.18	>21.9	37	51	68	37	765
EN2-06	>23.4	>24.94	>24.04	>23.18	>21.9	29	48	60	43	733
EN2-07	>23.4	>24.94	>24.04	>23.18	>21.9	29	38	56	<45	472
EN2-08	>23.4	>24.94	>24.04	>23.18	>21.9	34	44	57	42	685
EN2-09	>23.4	>24.94	>24.04	>23.18	>21.9	19	31	44	35	421
XMM-01	>25.0	>24.0	>24.2	>24.2	>23.6	47	72	99	74	1277
XMM-02	26.08	23.86	24.45	23.84	22.98	36	47	58	<66	1512
XMM-03	>25.0	24.39	24.36	22.32	21.41	70	77	93	58	1194
XMM-04	···	···	>24.2	···	···	47	63	113	95	1253
XMM-05	26.12	25.70	24.86	24.20	22.98	54	62	59	50	1398
XMM-06	>25.0	>24.0	>24.2	>24.2	>23.6	62	71	<58	<66	1109

Notes. Typical uncertainties are ∼5% for the optical and the IRAC data, and 10% for MIPS. Upper limits correspond to 90% completeness in the optical and to 5σ in the infrared.

Table 3
Statistical Information on MAMBO 1.2 mm Results

Sample	N	N			$< f_{1.2\,\mathrm{mm}}(All) >$	$< f_{1.2\,\mathrm{mm}}(\geqslant 2\sigma) >$[a]	$< f_{1.2\,\mathrm{mm}}(< 2\sigma) >$[b]
		$\geqslant 2\sigma$	$\geqslant 3\sigma$	$\gtrsim 4$ mJy	(mJy)	(mJy)	(mJy)
Total	61	21 (34%)	16	3	1.49 ± 0.18	2.90 ± 0.22	0.75 ± 0.14
LH	29	12 (41%)	9	3	1.88 ± 0.28	3.19 ± 0.36	0.95 ± 0.22
EN1+EN2+*XMM*	32	9 (28%)	7	0	1.14 ± 0.20	2.51 ± 0.12	0.60 ± 0.17

Notes. Uncertainties correspond to the standard deviation of the mean.
[a] Mean 1.2 mm flux density of sources with $f_{1.2\,\mathrm{mm}} > 2\sigma$.
[b] Mean 1.2 mm flux density of sources with $f_{1.2\,\mathrm{mm}} < 2\sigma$.

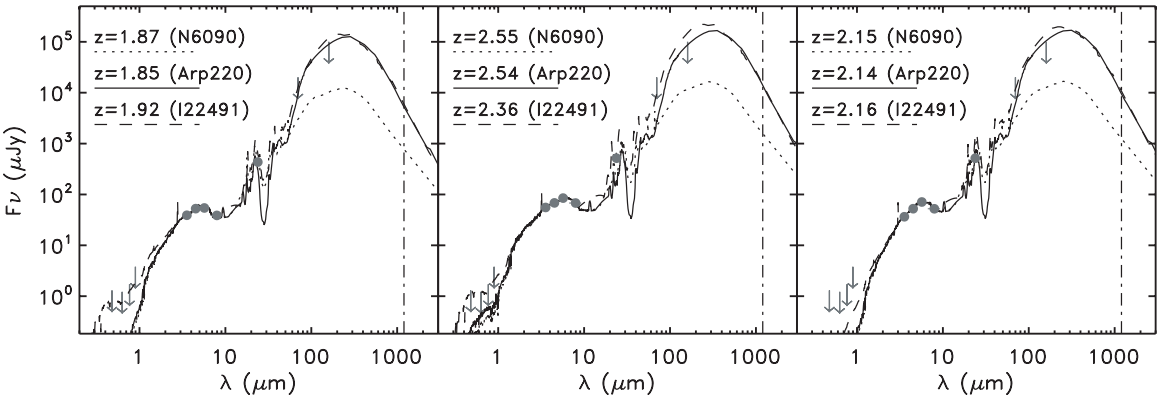

Figure 2. Fits of 3 SWIRE/MAMBO sources with the 3 starburst templates used to predict 1.2 mm flux densities, Arp 220 (solid curve), NGC 6090 (dotted curve), and I22491 (dashed curve). Downward arrows represent 5σ upper limits. The vertical dot-dashed line represents the 1.2 mm wavelength.

The starburst templates correspond to the SEDs of NGC 6090, NGC 6240, Arp 220, IRAS 20551−4250, and I22491 (Silva et al. 1998; Berta 2005). The composite (AGN+SB) template corresponds to the SED of the Seyfert 2 galaxy IRAS 19254−7245 South (I19254; Berta et al. 2003). A description of the library and of the method can be found in Polletta et al. (2007).

We fit the SEDs using the data up to 24 μm, including upper limits. Although the optical upper limits place some constraints on the acceptable fits, for these optically faint objects the photometric redshifts are based primarily on the IRAC bands. The photometric redshifts are therefore limited in accuracy by (1) the small number of available photometric bands (3–4 IRAC bands, MIPS[24], and up to a maximum of 5 optical bands among *Ugriz*), and (2) the fact that the main spectral feature available for fitting (the peak in the stellar spectrum) is broad and detected through broad filters. Therefore our photometric redshifts are expected to have uncertainties of ± 0.5 in redshift or higher, even for the highest SNR sources. In order to illustrate the range of acceptable solutions and photometric redshifts, we report multiple solutions if they give similar χ^2. The fits were also done without including the 24 μm measurements. Since the comparison with spectroscopic redshifts was slightly better when those data were included, we decided to adopt the results obtained using also the 24 μm data. The inclusion of 24 μm data in the fitting procedure can yield better results, if templates including dust emission, like the libraries used here, are employed (see e.g., Polletta et al. 2007).

The reliability and accuracy of the photometric redshifts can be estimated using the available spectroscopic data. Spectroscopic redshifts from the IRS are available for 8 sources and are listed in Table 1 (Weedman et al. 2006, C. J. Lonsdale et al. 2009, in preparation). We define the fractional error Δz, the systematic mean error $\overline{\Delta z}$, the 1σ dispersion σ_z, and the rate of catastrophic

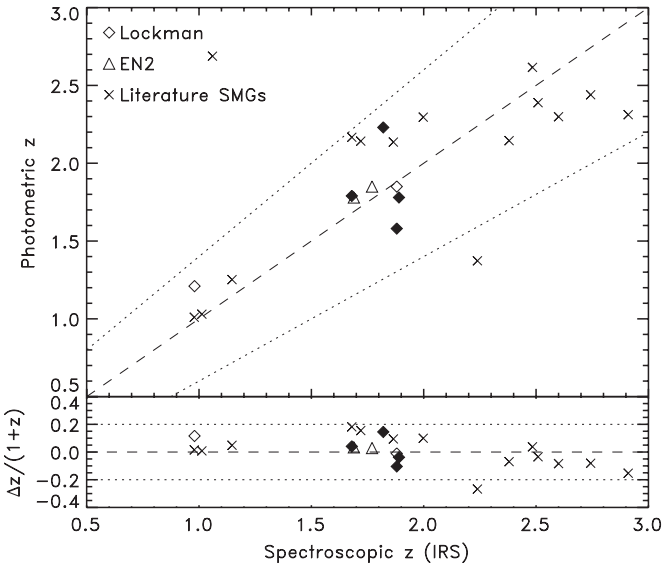

Figure 3. Comparison between photometric and spectroscopic redshifts from IRS (C. J. Lonsdale et al. 2009, in preparation Weedman et al. 2006) of the 8 SWIRE/MAMBO sources with available spectroscopic redshifts (diamond and triangles). Dotted lines represent 20% agreement in $(1+z)$. Full symbols represent sources with $f_{1.2\,\mathrm{mm}} > 2\sigma$, and empty symbols sources with $f_{1.2\,\mathrm{mm}} < 2\sigma$. Diamonds represent LH sources, and triangles sources in the other three SWIRE fields. Crosses represent 15 sources from the literature sample of SMGs with available spectroscopic redshifts, a 24 μm detection, and exhibiting a peak in the IRAC bands.

outliers, defined as the fraction of sources with $|\Delta z| > 0.2$. Δz is defined as:

$$\Delta z = \left(\frac{z_{\mathrm{phot}} - z_{\mathrm{spec}}}{1 + z_{\mathrm{spec}}} \right) \quad (1)$$

and

$$\sigma_z^2 = \sum \left(\frac{z_{\rm phot} - z_{\rm spec}}{1 + z_{\rm spec}} \right)^2 \Big/ N \qquad (2)$$

with N being the number of sources with spectroscopic redshifts. The systematic mean error, $\overline{\Delta z}$, is 0.03. The *rms* of $\overline{\Delta z}$, σ_z is 0.08, and there are no outliers with $|\Delta z| > 0.2$. The comparison between the spectroscopic and final photometric redshifts is shown in Figure 3 for the eight sources. There is a good agreement for five sources, and for three sources there is a difference $\gtrsim$0.05 in $\log(1 + z)$. In order to better asses the reliability of our estimates, we applied the same technique to a sample of 24 μm detected SMGs from the literature with known spectroscopic redshift and with at least three detections in the IRAC bands consistent with the presence of a peak at either 4.5 μm or 5.8 μm. We found 15 sources that satisfy these criteria out of the 90 SMGs for which we collected data from the literature (see Section 1). Note that most of the sources from the literature do not benefit from observations from as many bands as the SWIRE-MAMBO sample. After combining the SWIRE-MAMBO and the literature sample, $\overline{\Delta z} = 0.03$, $\sigma_z = 0.19$, and we find two outliers ($|\Delta z| > 0.2$), corresponding to ~9% of the sample. The results obtained for the literature sample confirm the accuracy of our estimates on the SWIRE-MAMBO sample.

SED fits for all the SWIRE sources in the sample are provided in the Appendix and the best-fit templates and photometric redshifts are listed in Table 4.

The redshift distribution of the sample, based on the photometric redshifts (solid line) and on the spectroscopic redshifts (dotted line) when available, is shown in Figure 4. The distribution peaks at $z \simeq 2.0$, which corresponds to about the minimum redshift for a 5.8 μm peaker. The z peak of our sources is slightly lower than the redshift distribution of submillimeter-selected sources (Frayer et al. 2004b; Egami et al. 2004; Borys et al. 2005; Chapman et al. 2005; Greve et al. 2004). Note that the difference could be even larger because of the possible overestimate of $z_{\rm phot}$ in case, for example, of a shift of the peak of the stellar bump due to an AGN contribution (e.g., a 'b2' can appear as a 'b3' and its redshift be overestimated by $\Delta z = 1$; see e.g., Berta et al. 2007b; Daddi et al. 2007).

6. GENERAL PROPERTIES OF THE SWIRE-MAMBO SOURCES

6.1. Millimeter and 24 μm Fluxes

The distribution of observed 1.2 mm flux densities (separated in sources with $f_{1.2\,\rm mm} \geqslant 2\sigma$ and $< 2\sigma$) is illustrated in Figure 5. The fraction of $> 2\sigma$ sources, 41% (24% at 4σ), and the large average 1.2 mm flux observed in our samples (1.5 ± 0.2 mJy), and especially in the more thoroughly observed LH sample (1.9 ± 0.3 mJy), show that our criteria are quite successful in selecting submillimeter-bright galaxies from MIR samples.

The *XMM*, EN1 & EN2 sample show systematically lower fluxes compared to the LH sample. Although the LH sample was more thoroughly observed than the other samples, with typical exposure times >1.5 hr, compared to ~40 minutes for the other sources, the origin of the different detection rate and average fluxes is more likely due to intrinsic properties of the sources or of the fields, e.g., cosmic variance, than to the observational parameters. The most plausible explanation is that our selection introduced different biases in the selected samples possibly due to the different optical coverage or to the analysis carried out on the SEDs and on the images during the source selection process. The latter was indeed more extensive in the LH field.

Table 4
Best-fit Templates and Photometric Redshifts

Source ID	z	A_V	Template
LH-01	1.345	1.43	SBSey
LH-02	1.925	1.69	ce_96
	1.934	1.95	N6090
LH-03	2.674	1.04	I22491
	2.332	0.26	ce_81
LH-04	2.943	1.04	I20551
LH-05	1.583	0.39	ce_86
	1.734	1.04	spi1_4
LH-06	1.791	0.78	ce_76
	1.803	1.56	I22491
LH-07	2.225	1.17	I22491
LH-08	2.014	0.78	ce_66
	2.035	1.04	Arp220
LH-09	2.283	0.91	I20551
LH-10	2.234	1.43	I20551
LH-11	1.661	0.52	ce_105
	1.848	1.43	spi2c_3
LH-12	1.783	0.00	ce_81
	2.652	0.65	I22491
LH-13	1.699	0.26	ce_96
LH-14	2.032	1.17	I22491
	2.158	0.39	ce_81
LH-15	2.804	0.39	ce_81
	3.235	0.78	I20551
LH-16	2.406	0.13	I19254
	2.450	1.95	I22491
LH-17	1.850	0.52	N6090
LH-18	2.164	1.95	N6090
LH-19	2.111	1.82	N6090
	2.359	1.04	I20551
LH-19	2.362	0.65	ce_86
LH-20	1.896	1.43	N6090
	1.990	0.52	ce_76
	1.945	0.52	ce_96
LH-21	2.630	0.39	ce_81
	2.915	0.65	I20551
LH-22	1.535	1.04	ce_76
	1.831	0.78	I22491
LH-23	1.207	1.95	ce_86
LH-24	1.254	1.43	SBSey
	1.756	1.17	I22491
LH-25	2.133	1.43	I20551
	2.180	1.56	N6090
LH-26	1.853	1.95	ce_81
LH-27	2.014	0.52	I22491
	2.108	0.00	ce_81
LH-28	2.815	0.65	I22491
LH-29	2.164	1.69	N6090
	2.342	1.04	I20551
EN1-01	2.369	1.69	I20551
EN1-02	1.934	1.95	N6090
	1.999	1.43	ce_91
EN1-03	1.896	1.95	N6090
	2.002	0.91	ce_86
EN1-04	2.002	0.91	I22491
	2.136	0.13	ce_81
EN1-05	1.879	0.26	ce_81
EN1-06	2.366	1.95	N6090
	2.699	1.17	I20551
EN1-07	1.397	1.95	ce_71
	1.836	0.65	N6090
EN1-08	2.026	1.95	N6090
	2.127	1.95	ce_81
EN1-09	1.685	0.91	N6090
	1.867	0.78	ce_66
EN1-10	2.379	1.95	N6090
	2.744	1.30	I20551

Table 4
(Continued)

Source ID	z	A_V	Template
EN1-11	1.545	1.95	I20551
	3.500	0.00	N6240
EN1-12	2.111	1.95	N6090
	2.299	1.30	ce_81
EN1-13	1.945	1.95	N6090
	2.164	1.04	ce_81
EN1-14	2.392	1.95	N6090
EN1-15	1.960	1.95	N6090
	2.205	0.91	ce_81
EN1-16	2.221	1.04	ce_81
	2.594	1.04	I22491
EN1-17	2.152	1.95	N6090
	2.342	1.95	I20551
EN2-01	1.848	0.78	ce_91
	1.969	1.04	I22491
EN2-02	1.570	1.95	ce_96
EN2-03	1.853	1.69	ce_81
	1.934	1.95	N6090
EN2-04	1.775	0.26	ce_91
	1.876	1.04	spi1_4
EN2-05	2.056	1.17	I22491
	2.077	1.04	ce_86
EN2-06	1.951	1.95	I22491
	2.008	1.95	ce_91
EN2-07	2.152	1.95	N6090
	2.339	1.30	I20551
	2.450	1.04	ce_86
EN2-08	1.960	1.95	N6090
	2.087	1.17	I22491
	2.174	1.04	ce_81
EN2-09	2.180	1.95	N6090
	2.273	1.95	ce_91
	2.299	1.95	I20551
XMM-01	1.890	1.95	ce_81
	1.972	1.95	N6090
XMM-02	1.928	0.00	ce_81
	2.273	0.78	I22491
XMM-03	2.113	0.00	N6090
	1.413	0.00	N6090
XMM-04	2.124	1.95	ce_81
	2.212	1.95	N6090
XMM-05	1.010	1.82	SBSey
	1.147	1.17	ce_86
	1.778	0.13	N6090
XMM-06	1.010	1.95	M82
	1.205	1.82	ce_86

Notes. The solutions are listed in order of χ^2. All the 'ce' templates are from the library in Chary & Elbaz (2001), the others are from the library in Polletta et al. (2007). The fits are shown in Figure 13.

In Figure 5, we also show the distribution of 1.2 mm fluxes of the 90 SMGs selected from the literature (see Section 2). In case of lack of flux measurement at 1.2 mm for the SMGs from the literature, we estimate it from the flux at 850 μm by applying the following equation:

$$\mathrm{Log}(f_{1.2\,\mathrm{mm}}) = -0.36 + 0.98 \times \mathrm{Log}(f_{850\,\mu\mathrm{m}}) \quad (3)$$

where $f_{1.2\,\mathrm{mm}}$ and $f_{850\,\mu\mathrm{m}}$ are the flux densities at 1200 and 850 μm, respectively. This relationship is derived from a sample of 21 SMGs for which measurements at both 850 and 1200 μm are available (Greve et al. 2004).

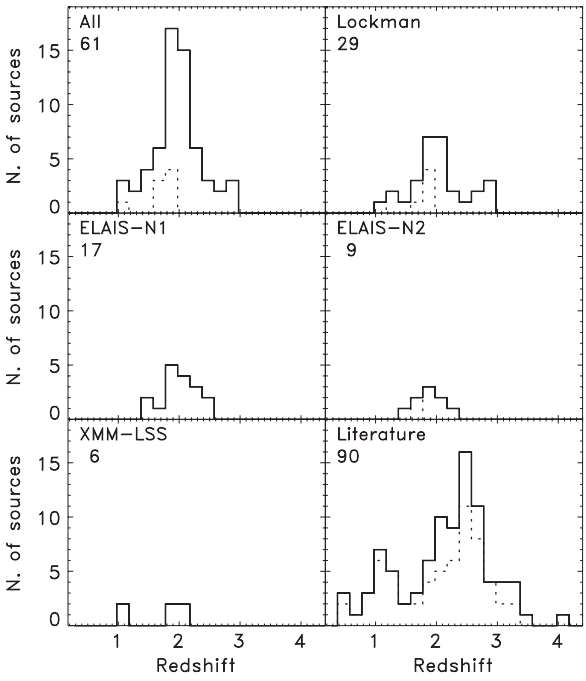

Figure 4. Redshift distribution for all observed sources. The distribution of spectroscopic redshifts is shown with a dotted line. From top to bottom and from left to right, all MAMBO/SWIRE sources, those in the Lockman Hole, ELAIS-N1, ELAIS-N2, and *XMM*-LSS, and from the literature (Egami et al. 2004; Borys et al. 2005; Chapman et al. 2004; Greve et al. 2004; Pope et al. 2006). The number of sources is annotated on the upper left corner of each panel.

Based on Figure 7 in Voss et al. (2006) and the 850 μm source counts from SHADES (Coppin et al. 2006), the expected number of SMGs with $f_{1.2\,\mathrm{mm}}$ >5 mJy, 4 mJy, and 3 mJy in the 9 deg^2 LH field is ~250, 800, and 2,000, respectively. On the other hand, we have identified only two, three, and four sources brighter than 5 mJy, 4 mJy, and 3 mJy, respectively out of 29 24 μm bright sources in the 9 deg^2 LH field. Accounting for the fact that we have sampled with MAMBO ~5.6% of the LH 5.8 μm peakers which are brighter than 400 μJy at 24 μm, we find that we are detecting about 15% of the predicted number of SMGs brighter than 5 mJy. The small number of mm-bright sources in our sample and in the sample in Lutz et al. (2005) suggests that very luminous millimeter sources are not common among sources with bright 24 μm fluxes ($f_{24\,\mu\mathrm{m}} > 400$ μJy).

In Figure 6, we show the distribution of 24 μm fluxes of the SWIRE-MAMBO sample and of the SMGs from the literature. All SWIRE-MAMBO sources have 24 μm greater than 400 μJy as imposed by the selection criteria. The 24 μm fluxes of our sample range from 0.4 to 1.5 mJy, with a median value of 0.76 mJy and a mean value of 1.09 $\pm$ 1.06 mJy. The SWIRE-MAMBO sources with $f_{1.2\,\mathrm{mm}} < 2\sigma$ show a similar range of 24 μm fluxes, but fewer of the faintest 24 μm sources are detected by MAMBO. Figure 6 clearly illustrates that the majority of SMGs are characterized by 24 μm fluxes smaller than 400 μJy. More specifically, out of the 90 SMGS from the literature, 20 (22%) have 24 μm fluxes greater than 400 μJy. Therefore, about 78% of classical SMGs would be missed by our selection criteria. Indeed, more than half of SMGs at $z \sim 2$ are not detected at the SWIRE sensitivity at 24 μm, ~250 mJy (and even at 5.8 or 8.0 μm, see Section 1). The lowest 24 μm flux in the SMGs reaches 21 μJy, but there are 16 sources that are not detected, four in GOODS ($f_{24\,\mu\mathrm{m}} <$ 26–50 μJy) and the others

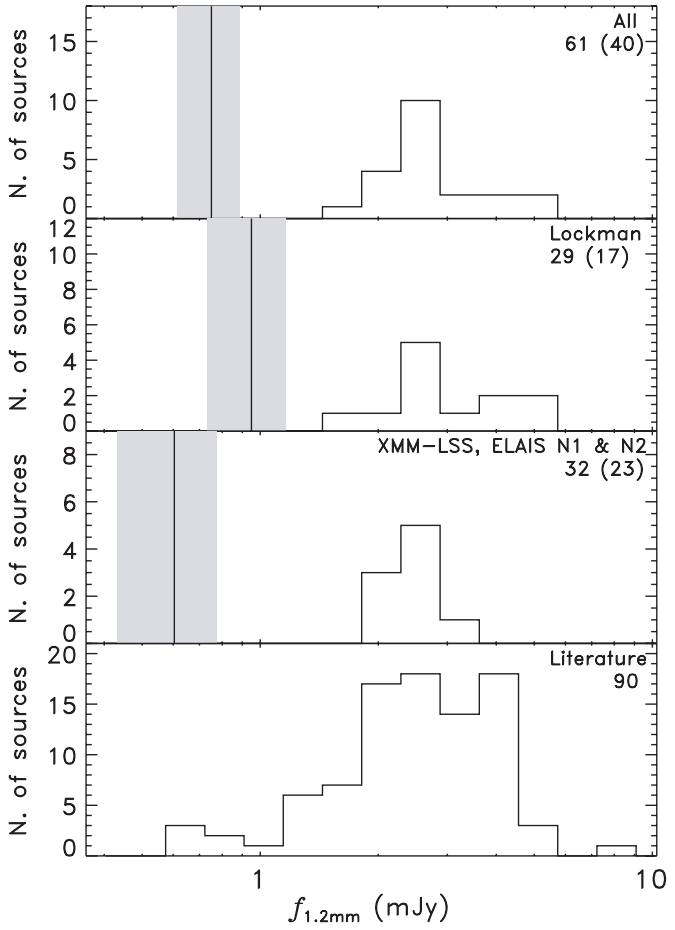

Figure 5. 1.2 mm flux distribution of sources with $f_{1.2\,\mathrm{mm}} > 2\sigma$ (histogram). The mean and mean standard deviation of the sources with $f_{1.2\,\mathrm{mm}} < 2\sigma$ are shown as a vertical solid line and a gray shaded area. From top to bottom, all MAMBO/SWIRE sources, those in the Lockman Hole, those in the the other fields, and those in the literature (Frayer et al. 2004b; Egami et al. 2004; Borys et al. 2005; Chapman et al. 2004; Greve et al. 2004; Pope et al. 2006). The total number of plotted sources is annotated and in parenthesis the number of sources with $f_{1.2\,\mathrm{mm}} < 2\sigma$ is given.

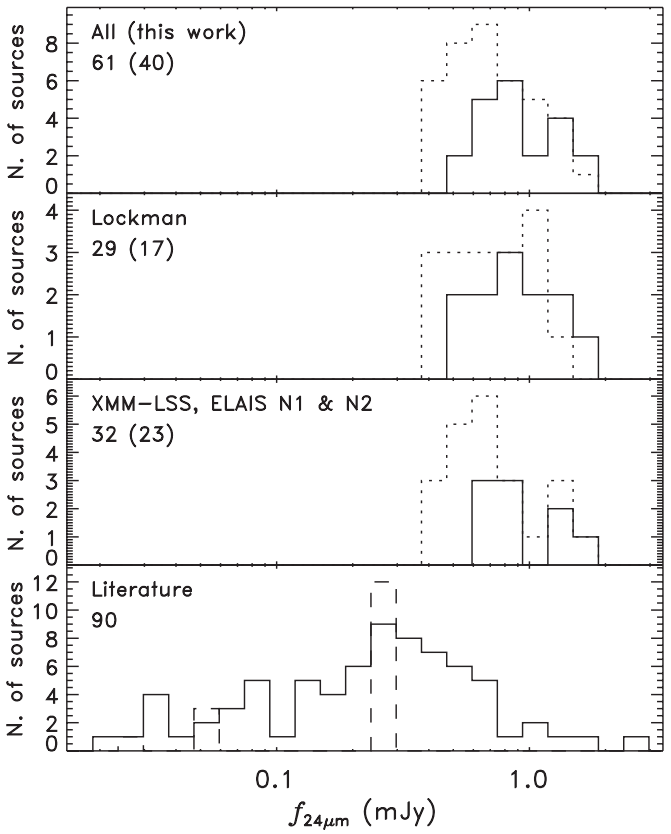

Figure 6. 24 μm flux distribution of sources with $f_{1.2\,\mathrm{mm}} > 2\sigma$ (solid line) and with $f_{1.2\,\mathrm{mm}} < 2\sigma$ (dotted line). From top to bottom, all MAMBO/SWIRE sources, those in the Lockman Hole, those in the the other fields, and those in the literature (Frayer et al. 2004b; Egami et al. 2004; Borys et al. 2005; Chapman et al. 2004; Greve et al. 2004; Pope et al. 2006). The dashed histogram represents the literature sources that are not detected at 24 μm for which we assumed a 5σ upper limit (250 μJy for 12 sources in the SWIRE fields, and 26 μJy for 1 GOODS SMG, and 506 μJy for 3 more GOODS SMGs). The total number of sources is annotated on the upper left corner in each panel. The value in parenthesis represents the number of sources with $f_{1.2\,\mathrm{mm}} < 2\sigma$.

in the SWIRE fields ($f_{24\,\mu\mathrm{m}} < 250$ μJy). Since our sources are at similar redshifts and show similar mm fluxes to SMGs, they either represent a subset of 24 μm bright SMGs (∼20%) or a different class of SMGs with enhanced MIR emission. This question will be further investigated in the following sections.

6.2. Comparison with Other Spitzer Samples

A number of works have recently been published about the MIR properties of SMGs. They are based on hundreds of sources detected both with *Spitzer* from 3.6 to 24 μm and with SCUBA at 850 μm or with MAMBO at 1.2 mm (see Section 2). Most of these sources have been identified in deep fields mapped both with SCUBA or MAMBO and *Spitzer* (Egami et al. 2004; Ivison et al. 2004; Greve et al. 2004; Chapman et al. 2005; Borys et al. 2003; Pope et al. 2005, 2006; Ivison et al. 2007; Yun et al. 2008), or in pointed *Spitzer* observations at the position of known SCUBA or MAMBO sources (Charmandaris et al. 2004; Frayer et al. 2004a, 2004b; Ashby et al. 2006; Valiante et al. 2007; Menéndez-Delmestre et al. 2007; Pope et al. 2008). All these studies focus on submillimeter or mm selected galaxies, while our *Spitzer* selection aims at sources bright at 24 μm. However, it is interesting to note that our sources satisfy the selection criteria based on IRAC colors developed to select SMG candidates among the IRAC population (see Equation (1) in Yun et al. 2008).

Only a few other studies have a similar approach to ours in characterizing the millimeter properties of *Spitzer* mid-IR selected sources. Lutz et al. (2005) study a sample of bright ($f_{24\,\mu\mathrm{m}} \gtrsim 1$ mJy) sources with high 24 μm/optical flux ratios, and $f_{24\,\mu\mathrm{m}}/f_{8\,\mu\mathrm{m}}$ flux ratios to favor star-forming galaxies, but which ended up to be largely contaminated by AGNs (Yan et al. 2005, 2007; Sajina et al. 2007). Others study AGN-dominated samples in the SWIRE survey (Polletta et al. 2008, I. Perez-Fournon et al. 2009, in preparation). The SWIRE-MAMBO sample differs from those studies because special care was applied to favor star forming galaxies and remove AGNs that usually dominate the population of 24 μm bright and optically faint sources (Brand et al. 2006). Since the presence of a bump in the rest-frame NIR is due to stellar emission, our selection disfavors sources with dominant AGN emission in the MIR. Our selection thus makes this sample unique with respect to other *Spitzer*-selected samples that have been followed-up at submillimeter and mm wavelengths

6.3. Spectral Energy Distributions

The spectral energy distributions (SEDs) of our sources are compared with those of submillimeter selected SMGs in

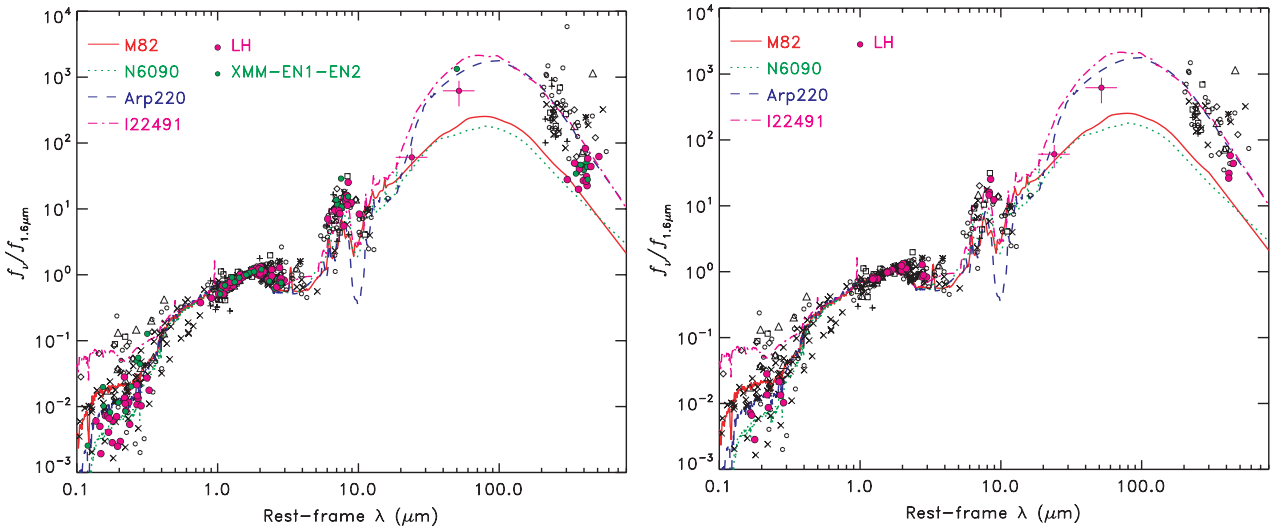

Figure 7. Rest-frame SEDs of SMGs from the literature (black symbols as in Figure 1) and of the SWIRE/MAMBO sources with 1.2 mm fluxes $> 2\sigma$ (full circles, red: Lockman Hole, green: *XMM*-LSS, ELAIS-N1, or ELAIS-N2) normalized at 1.6 μm. The 70 and 160 μm fluxes correspond to the normalized stacked fluxes of all SWIRE/MAMBO sources with 1.2 mm fluxes $> 2\sigma$. The curves represent starburst templates: M 82 (solid red), NGC 6090 (dotted green), Arp 220 (dashed blue), and I22491 (dot-dashed magenta). All sources are shown on the left panel and only sources with a spectroscopic redshifts are shown on the right panel.

Figure 7. Only sources with spectroscopic redshifts are shown in the right panel. All SEDs are shown in the rest-frame and normalized at 1.6 μm in the rest frame. The SWIRE sources are predominantly high in the 24 μm band at the location of the rest-frame 7.7 μm PAH emission feature, and low in the rest-frame FIR compared to the SMGs from the literature. The FIR emission of the SWIRE sources is in between that expected for the typical starburst galaxies as M 82, and NGC 6090, and a ULIRG like Arp 220, after normalizing them at the 1.6 μm in the rest-frame.

Figure 7 shows clearly the selection bias that is present in our sample: by selecting the 24 μm-brightest sources with a peak at 5.8 μm, we have strongly favored sources at $z \sim 2$ with large NIR and MIR luminosities. The classical SMG sample is naturally more biased towards the most mm-bright systems. The location of our sources in Figure 7 with respect to various template tracks confirms that their SEDs are intermediate between M 82 and Arp 220.

6.4. Colors and Nature of the Sources

We compare the 1.2 mm/24 μm flux ratio of the SWIRE and literature SMG samples in Figure 8. The SWIRE sources show on average lower flux ratios than the literature sources at the same redshift. The difference in the 1.2 mm/24 μm can not be simply explained by a redshift difference but is likely due to an excess in the MIR (i.e., 24 μm) with respect to the FIR in the SWIRE sample compared to the literature sample. Such an excess, also visible in the SEDs (see Figure 7), might be due to an AGN contribution in the MIR, or to enhanced PAH emission, or to a deficiency at mm wavelengths due to lower SFRs or higher temperatures. Indeed objects characterized by warmer dust temperatures are expected to show lower flux ratios (e.g., Chapman et al. 2003; Lewis et al. 2005).

In Figure 8, we also show for comparison the 1.2 mm/24 μm flux ratios measured in the sample of composite sources from Lutz et al. (2005), and in high-z radio galaxies (HzRG) detected at both 850 μm and 24 μm (Seymour et al. 2007). The 1.2 mm flux is derived from the 850 μm by applying equation 3. These two samples, from Lutz et al. (2005), and Seymour et al. (2007), show even smaller 1.2 mm over 24 μm flux ratios. In this case, the most plausible explanation for such small ratios is the contribution from AGN-heated hot dust emission to the MIR since both samples contain mainly AGNs. Since our sources show intermediate flux ratios in between those seen in the literature SMGs and HzRGs, it is quite possible that an AGN contributes to their MIR, more than typically observed in SMGs and less than observed in HzRGs.

To better investigate the origin of such an excess we consider in more detail the SMGs that fall in the same region covered by the SWIRE sources, and analyze the MIR spectra when available. From the literature subsample with available spectroscopic redshifts and available 24 μm flux (65 sources), we find three sources that fall in the same region in the $f_{1.2\,\mathrm{mm}}/f_{24\,\mu\mathrm{m}}$ *vs* z diagram as our sources, J123635.59+621424.1 ($f_{1.2\,\mathrm{mm}}/f_{24\,\mu\mathrm{m}} = 1.35$) at $z = 2.005$ from the GOODS North field (Borys et al. 2005), CSMM J163650+4057 ($f_{1.2\,\mathrm{mm}}/f_{24\,\mu\mathrm{m}} = 3.07$) at $z = 2.384$ from the ELAIS-N2 field (Greve et al. 2004), and SMM J105238.19+571651.1 ($f_{1.2\,\mathrm{mm}}/f_{24\,\mu\mathrm{m}} = 3.34$) at $z = 1.852$ (Chapman et al. 2005). The first two sources are AGNs, their MIR SEDs are consistent with a power-law model, their optical spectra show broad emission lines, and one source is also a luminous X-ray source. The latter source is instead classified as starburst galaxy based on its optical spectrum, and it also shows the highest 1.2 mm/24 μm flux ratio of the three selected sources. This analysis thus reinforces the hypothesis that an AGN component might be responsible for the lower flux ratios observed in the SWIRE sample, but this is based on only 2 sources and their SEDs are very different from those of our sources as a dominating AGN component is clearly seen in the MIR.

The best and probably unique way to constrain the presence and the contribution of an AGN component in the MIR is to measure the equivalent width of the PAH features. A warm dust continuum due to AGN-heated hot dust will decrease their equivalent width (see e.g., Clavel et al. 2000; Valiante et al. 2007; Menéndez-Delmestre et al. 2007; Sajina et al. 2007; Desai et al. 2007). This measurement can be performed using MIR spectra.

Based on the IRS spectra of similar samples and the few available here, a significant AGN contribution is disfavored for the majority of our sample. MIR spectra from IRS are available only for eight sources in our SWIRE-MAMBO sample

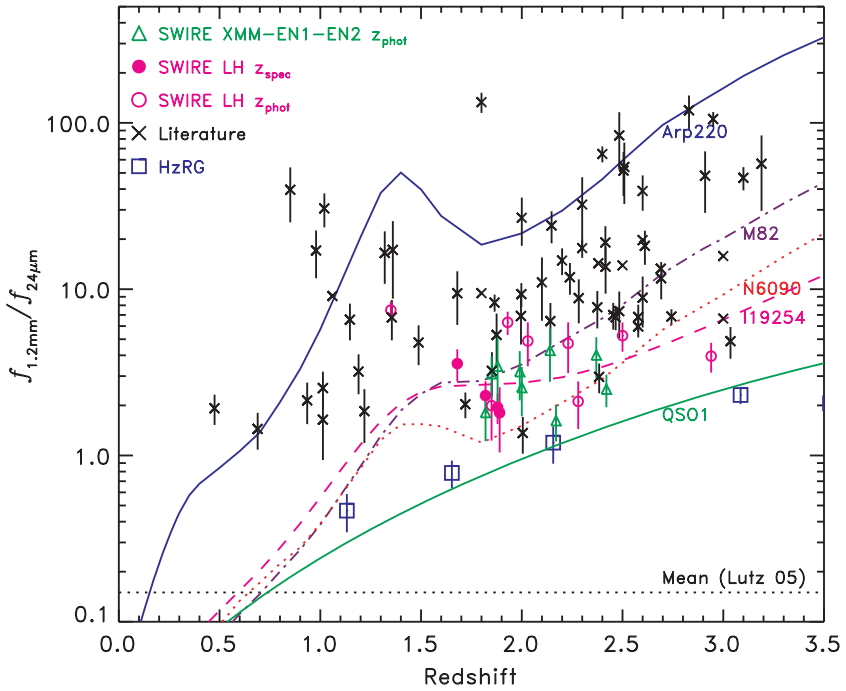

Figure 8. Observed flux ratios, $f_{1.2\,\mathrm{mm}}/f_{24\,\mu\mathrm{m}}$, as a function of redshift for SMGs from the literature (black crosses), for SWIRE/MAMBO sources with $f_{1.2\,\mathrm{mm}} > 2\sigma$ (circles: LH, triangles: other fields), and for high-z radio galaxies (blue squares: Seymour et al. 2007). Expected values for various starburst and AGN templates are also shown: Arp 220 (solid blue), M 82 (dot-dashed purple), NGC 6090 (dotted red), I19254 (dashed magenta), and QSO1 (dot-dot-dot-dashed green). Filled symbols represent SWIRE/MAMBO sources with spectroscopic redshifts, open symbols represent sources with photometric redshifts. Redshift uncertainties are not reported for clarity, but they are of the order of 0.5 for the photometric redshifts, and < 0.1 for the spectroscopic redshits. $f_{1.2\,\mathrm{mm}}$ fluxes for the literature sample are derived from $f_{850\,\mu\mathrm{m}}$ when not available. The average 1.2 mm/24 μm flux ratio of 24 μm-selected galaxies (Lutz et al. 2005) is shown as a dotted horizontal black line.

(A color version of this figure is available in the online journal.)

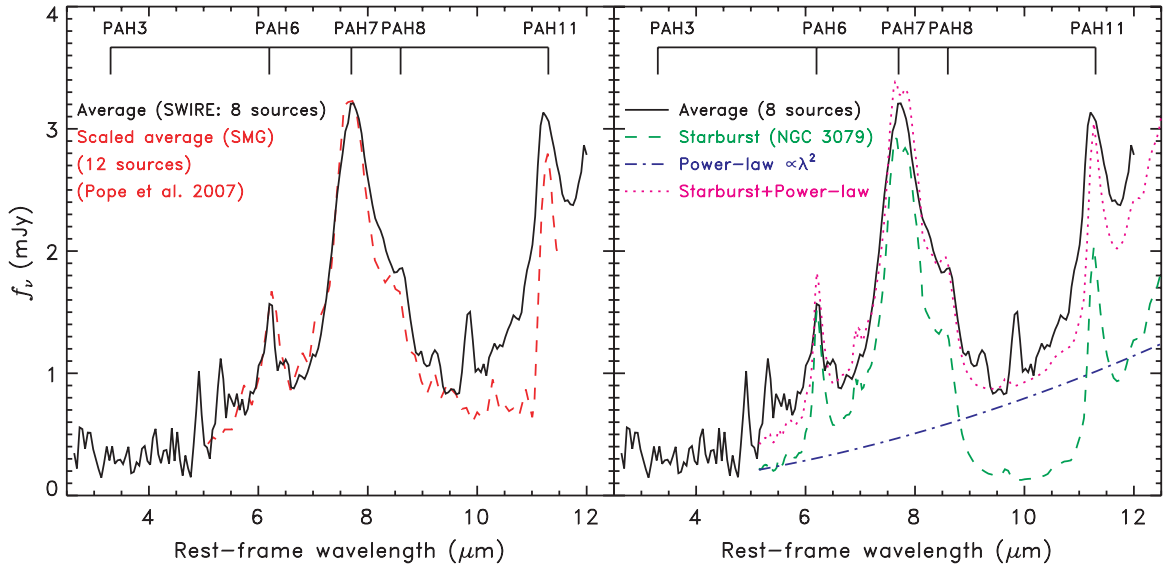

Figure 9. Average IRS spectrum of the eight SWIRE sources with available IRS spectra (black solid curve). Left panel: Also shown the composite spectrum of 12 SMGs from the HDFN (Pope et al. 2008) after scaling it to match the SWIRE average spectrum (red dashed curve). Right panel: IRS spectrum of a starburst (NGC 3079; green dashed curve), a power law model with spectral index 2 representing warm dust continuum emission (blue dot-dashed curve), and the sum of the two (magenta dotted curve). The expected locations of PAH emission features are labeled in both panels.

(A color version of this figure is available in the online journal.)

(Weedman et al. 2006, C. J. Lonsdale et al. 2009, in preparation). Altogether, six out of these eight sources show PAH dominated spectra and weak or absent continuum, implying large equivalent widths and negligible or absent AGN contribution. They are, in approximate order of PAH strength, LH-07, LH-06, LH-26, EN2-04, LH-12, and LH-05. The only exceptions are two sources (LH-23/B6, and EN2-03) that show, in addition to PAH emission, a warm dust continuum that might be associated with an AGN component. We do not find any trend between the presence of continuum, the strength of the PAHs, the 1.2 mm flux, and the $f_{1.2\,\mathrm{mm}}/f_{24\,\mu\mathrm{m}}$ flux ratio. Therefore, for this analysis we consider the average spectrum of all eight sources, independently of their properties. The average IRS spectrum of all eight SWIRE-MAMBO sources is shown in Figure 9. We also show

for comparison the composite spectrum of 12 SMGs from the Hubble Deep Field North (HDFN) (Pope et al. 2008), the IRS spectrum of a starburst, NGC 3079 (Weedman et al. 2005), a power-law model representing emission from warm dust, and the sum of the starburst spectrum and of the warm dust continuum. The average spectrum of the SWIRE-MAMBO sources clearly shows PAH features, implying a strong starburst component, but also a warm dust continuum. The average spectrum is well reproduced by the sum of the starburst spectrum and the warm dust continuum. The continuum is modeled with a power-law model ($f_\nu \propto \lambda^{\alpha_{IR}}$), with spectral index $\alpha_{IR} = 2$. We have applied the same analysis to the average spectrum after removing the 2 sources with larger continuum contamination and for the sources with $>2\sigma$ and $<2\sigma$ 1.2 mm fluxes and the result is still valid with only small differences that would require a larger sample to better quantify. The contribution of the power-law component to the average spectrum is ∼34% in the 6–12 μm rest-frame wavelength range. Assuming that the 24 μm flux includes a 34% contribution from an AGN on average, the AGN-subtracted $f_{1.2\,\mu m}/f_{24\,\mu m}$ flux ratio would be 1.5 times higher. Even after such a correction, our sources remain systematically on the lower bound region of the flux ratio distribution. Note that for consistency we would have to apply a similar correction to the literature SMGs as well. Indeed, the majority of classical SMGs also show both PAH features and a weak warm dust continuum in their MIR spectra (Valiante et al. 2007; Menéndez-Delmestre et al. 2007; Pope et al. 2008). The PAH equivalenth withs of our sources and of classical SMGs are in fact very similar, as shown in the left panel of Figure 9. Thus, the hypothesis that our sources might have an enhanced 24 μm flux due to the contribution from AGN emission, is disfavored. However, our sources are more luminous at 24 μm than SMGs. Their PAHs and MIR continuum are thus, on average, more luminous than in SMGs.

7. FAR-INFRARED PROPERTIES

In order to estimate FIR luminosities, and star formation rates (SFRs) of the SWIRE-MAMBO sources, their FIR SEDs need to be characterized. Since most of the sources are too faint to be detected at 70 and 160 μm with MIPS at the SWIRE sensitivity (typically 18, and 108 mJy, respectively), we can only use the observed 1.2 mm flux and make reasonable assumptions about their FIR SEDs. We assume that the FIR–mm emission of our sources is similar to that seen in SMGs, and model their FIR–mm emission with a greybody model normalized at the observed 1.2 mm flux, or 3σ upper limit if the flux is $<2\sigma$. To constrain the temperature of the FIR–mm emitting dust, it would be necessary to have at least two flux measurements at FIR–mm wavelengths. Since the dust temperature can not be directly estimated for our sources, we fix the temperature to the values typically observed in SMGs after taking into account the dependency of the dust temperature on the redshift. From the sample of SMGs with multiple submillimeter and mm data studied by Kovács et al. (2006), we derive:

$$T_{\rm dust} = 3.9 + 9.5 \times (1 + z) \quad (K). \tag{4}$$

We use a dust emissivity index $\beta = 1.5$ as in Kovács et al. (2006). Higher values of β give slightly larger temperatures (see Figure 3 in Kovács et al. 2006), and larger FIR luminosities. At parity of flux and temperature, the FIR luminosity derived with $\beta = 2$ is on average 2.3 times larger than the FIR luminosity derived with $\beta = 1.5$. Two submillimeter/mm flux measurements are available only for 4 sources in our sample (A. Kovacs et al. 2009, in preparation). In these four cases, the estimated temperatures are consistent with the measured ones, giving support to our assumption. The dust temperatures range from 23 K to 41 K, with a mean value of 33 ± 4 K. In order to take into account the redshift uncertainty, the greybody fits are performed three times: (1) at the best redshift of the source, $z_{\rm best}$; (2) at a lower redshift, $z_- = z_{\rm best} - 0.12 \times (1 + z_{\rm best})$; and (3) at a higher redshift, $z_+ = z_{\rm best} + 0.12 \times (1 + z_{\rm best})$. The coefficient 0.12 corresponds to 1.5 times the dispersion found in the comparison between photometric and spectroscopic redshifts (see Section 5). The FIR luminosities are reported in Table 5. The FIR luminosities for the sources with a $> 2\sigma$ signal at 1.2 mm range from 1 to 6.3 × 10^{12} $L_\odot$, confirming that our SWIRE-MAMBO sources are ULIRGs. This is true for the majority of the sources also at $z = z_-$. A similar luminosity range is obtained for the rest of the sample, but they are likely upper limits to the true FIR luminosity.

The greybody models are always below the 70 μm, and 160 μm upper limits of each source, implying that the assumed temperatures are never overestimated. If the temperature of the fits were increased to come closer to the FIR upper limits, the estimated FIR luminosities would increase.

We carry out an additional analysis to characterize the average FIR SED of our sources. We estimate average fluxes at 70 μm

Table 5
FIR and NIR Luminosities and Dust Temperatures for the Lockman Hole Sample

Source ID	$T_{\rm dust}$ (K)	$\mathrm{Log}(L_{\rm FIR}^{GB})(z,z_-,z_+)$ ($L_\odot$)	$\mathrm{Log}(\nu L_{1.6\,\mu m})$ ($L_\odot$)
LH-01	26.25	12.23 (11.94, 12.46)	11.93
LH-02	31.76	12.62 (12.39, 12.79)	11.69
LH-03	38.79	12.80 (12.62, 12.93)	12.28
LH-04	41.36	12.75 (12.59, 12.87)	11.91
LH-05	31.29	12.33 (12.33, 12.33)	11.74
LH-06	29.39	12.32 (12.32, 12.32)	12.07
LH-07	30.72	12.27 (12.27, 12.27)	12.09
LH-08	32.53	12.34 (12.12, 12.51)	12.57
LH-09	35.09	12.31 (12.11, 12.47)	12.15
LH-10	34.62	12.40 (12.20, 12.56)	12.25
LH-11	29.20	12.04 (11.79, 12.23)	12.03
LH-12	31.39	12.28 (12.28, 12.28)	12.04
LH-13	29.58	⩽12.22 (11.97, 12.41)	12.58
LH-14	32.72	⩽12.44 (12.22, 12.60)	12.09
LH-15	40.03	⩽12.63 (12.46, 12.75)	11.96
LH-16	36.23	⩽12.63 (12.44, 12.78)	12.13
LH-17	31.00	⩽12.36 (12.13, 12.55)	11.86
LH-18	33.95	⩽12.53 (12.32, 12.69)	11.79
LH-19	33.47	⩽12.66 (12.45, 12.83)	12.06
LH-20	31.48	⩽12.35 (12.12, 12.53)	11.79
LH-21	38.42	⩽12.64 (12.46, 12.77)	12.21
LH-22	28.06	⩽12.36 (12.10, 12.57)	11.98
LH-23	22.74	⩽11.63 (11.63, 11.63)	10.76
LH-24	25.31	⩽12.06 (11.76, 12.30)	11.54
LH-25	33.67	⩽12.50 (12.29, 12.67)	12.58
LH-26	31.29	⩽12.31 (12.31, 12.31)	11.75
LH-27	32.53	⩽12.57 (12.35, 12.75)	11.92
LH-28	40.22	⩽12.87 (12.70, 12.99)	11.93
LH-29	33.95	⩽12.56 (12.35, 12.72)	11.44

Notes. $L_{\rm FIR}^{GB}$ is the integrated luminosity between 42.5 and 122.5 μm (Helou et al. 1988) obtained using a greybody model with $T_{\rm dust} = 3.9 + 9.5 \times (1 + z)$, and $\beta = 1.5$ (see text). The luminosities have been obtained at the redshift z of each source. In brackets are the luminosities derived at $z_+ = z + 0.12 \times (1 + z)$ and $z_- = z - 0.12 \times (1 + z)$.

Table 6
Results from the Co-added MIPS Images for the Lockman Hole Sample

Sample	N	$\langle f_{24}\rangle$ Detections Mean	f_{24} Stack Mean	f_{70} Stack Mean	f_{160} Stack Mean
		(mJy)			
All	27	0.83 ± 0.31	0.93 ± 0.08	5.7 ± 1.5	39.0 ± 10.2
$f_{1.2\,\mathrm{mm}} > 2\sigma$	12	0.92 ± 0.33	0.99 ± 0.11	5.7 ± 1.3	57.8 ± 16.3
$f_{1.2\,\mathrm{mm}} < 2\sigma$	15	0.75 ± 0.28	0.90 ± 0.11	7.3 ± 2.8	16.9 ± 8.2

and 160 μm by co-adding all the 70 μm and all the 160 μm images to create a stacked 70 μm image and a stacked 160 μm image. The co-adding technique used in this work follows the method described in Dole et al. (2006). This technique was applied to all MIPS images (24, 70, and 160 μm) and only to the sources in the LH field since the number of observed and detected sources is significantly larger than in the other fields. The stacking of the 24 μm images was carried out to validate the method by comparing the stacking result with the mean flux of the single measurements. In the rest of the analysis, we will use the mean of the single measurements at 24 μm instead of the stacking value. Two sources, LH-18, and LH-28, were excluded from the stacking because the former is located at the edge of the 160 μm image, and the latter is detected at 70 μm. We divided the remaining 27 sources in the Lockman Hole sample in two sub-groups: sources with 1.2 mm fluxes above 2σ (12), and below 2σ (15).

At each of the positions of the sources in each subgroup, we extract a $72'' \times 72''$ subimage from the full-field SWIRE mosaics. The subimages are placed into a stack twice, once with their original orientation, and again with a 90° rotation, to remove instrumental effects such as gradients affecting the stacked flux. However, since the MIPS maps are already filtered following the techniques described in Frayer et al. (2006), the rotation should not give a significant difference. Indeed, a test on the the 70 μm stacks with and without image rotation yields a difference of 1.4% which is negligible compared to the uncertainty. The mean flux image is computed from the stack, and the flux measured in an aperture (with sky subtraction in an annulus included). An uncertainty estimate is derived using a bootstrap technique (Efron & Tibshirani 1993), in which samples of the subimages are drawn with replacement from the image stack, and the mean image and aperture flux measurement are recomputed. The standard deviation of the aperture flux measurements of 200 repetitions of this process yields the uncertainty estimate. We have validated these uncertainty estimates by stacking positions randomly offset by 60 to 80 arcseconds from our source positions; the standard deviation of 500 such stacks is slightly lower than the uncertainties from the bootstrap method. All of the measured stacked fluxes are reported in Table 6. The mean of the single measurements at 24 μm agrees in all three cases with the stacked mean 24 μm flux, within the uncertainties.

The stack of all 27 LH sources results in a detection at both 70 and 160 μm, at $\sim 3.8\sigma$. The stack of sources $> 2\sigma$ 1.2 mm fluxes is well ($\sim 4\sigma$) detected at both wavelengths. The stack of the sample with $f_{1.2\,\mathrm{mm}} < 2\sigma$ does not result in a detection at either wavelength. Note that the significance level of these measurements reflects mainly differences in noise level due to small number statistics. However, these measurements provide some constraints on the average FIR flux and spectrum of our sources.

The average FIR SEDs (from 24 to 1200 μm, including the stacked 70 and 160 μm fluxes) of the LH subsample with $f_{1.2\,\mathrm{mm}} > 2\sigma$ is shown in Figure 10. The figure also shows the predicted average flux at 70 and 160 μm assuming the greybody models used to compute the FIR luminosities. The stacked mean fluxes are well above the greybody models predictions (solid black curve in Figure 10). This discrepancy cannot be explained by any of our uncertainty (in redshifts for example). At 160 μm the mean observed flux predicted by the greybody models is 4 times lower than measured in the stacked images. This discrepancy suggests that our sources are more FIR luminous and warmer than estimated by the greybody models that are based on the SMGs temperatures. In order to fit the SWIRE-MAMBO sources average FIR SED, the dust component should be on average 10 K higher than predicted. Indeed, a greybody model that fits the average FIR SED assuming the mean redshift of the LH sub-sample, $z = 2.03$, has a temperature of 42.5 K (dashed black curve in Figure), instead of 32.7 K as predicted by Equation (4). Note that while the excess at 160 μm can be explained by a temperature effect, at 70 μm ($\gtrsim$20 μm in the rest-frame) a different contribution from small grains is more likely. In this work, we do not investigate the difference at 70 μm, as we focus our analysis on the FIR part of the spectrum.

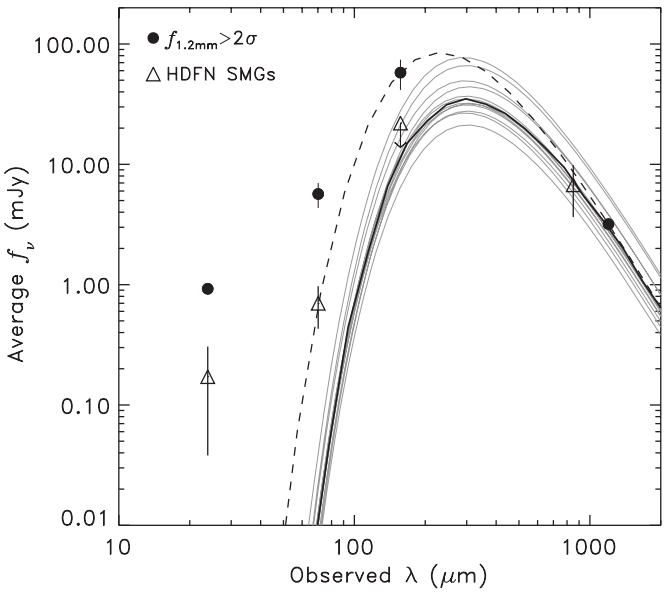

Figure 10. Average FIR SEDs of LH sources with $f_{1.2\,\mathrm{mm}} > 2\sigma$ (black full circles). The 70 μm and 160 μm average fluxes correspond to the stacked values. The grey curves represent redshifted greybody fits (see Equation (4)) of all 27 LH sources with $f_{1.2\,\mathrm{mm}} > 2\sigma$. The thick solid black line represents the median of all the greybody fits shown in the Figure as grey curves. The dashed black line represents a greybody model fit to the average 160 μm and 1.2 mm fluxes assuming the mean redshift, $z = 2.03$, and a temperature $T = 42.5$ K. As expected the median 1.2 mm flux of the models and observed are the same, but at 160 μm, the median model predicts a flux that is 4.9 times smaller than the measured value. The triangles at 24 μm and 850 μm represent the average observed fluxes of the sample of 31 HDFN SMGs (Pope et al. 2006), and the triangles represent the stacked fluxes at 70 μm and 160 μm of a subsample of 26 sources from the same sample (Huynh et al. 2007).

For comparison with the classical SMGs, we consider the FIR properties of >30 SMGs from the HDFN sample (Pope et al. 2006, 2008). The mean FIR SED of this sub-sample is also shown in Figure 10. The 850 μm fluxes of these SMGs range from 1.7 to 20.3 mJy (corresponding to 0.7–8.3 mJy at 1.2 mm), and show a mean value of 5.7 mJy (corresponding to 2.4 mJy at 1.2 mm), consistent with our SWIRE-MAMBO sources with $f_{1.2\,\mathrm{mm}} > 2\sigma$. Their average 70 and 160 μm fluxes,

derived from the stacking of a sub-sample of 26 sources by Huynh et al. (2007), are significantly lower than those measured in the SWIRE sample. Such a difference suggests that the HDFN SMGs are, on average, characterized by cooler dust temperatures and lower FIR luminosities. Note that the sub-sample used by Huynh et al. (2007) does not include 2 sources that are detected in the MIPS images. However, even including those sources the average FIR SED of classical SMGs would remain well below that of our sources.

In summary, the analysis of the average FIR SED of the SWIRE-MAMBO sources with $f_{1.2\,\mathrm{mm}} > 2\sigma$ indicates that their FIR luminosities are higher than estimated using the greybody models and that the FIR emitting dust is at higher temperatures than assumed. On average, our sources are thus more luminous and warmer than classical SMGs, given that the two samples have similar redshift distributions.

thus more luminous and warmer than classical SMGs.

8. STELLAR MASSES

Our IRAC-based selection corresponds to a rest-frame NIR selection, therefore, in absence of a significant AGN contribution at these wavelengths, we are directly sampling the stellar component. Moreover a NIR selection is minimally affected by dust extinction. Therefore it is possible to derive accurate stellar masses, by means of spectrophotometric synthesis. We focus this analysis on the better observed and larger LH sample.

We use the code Sim-Phot-Spec (SPS), developed in Padova (Berta et al. 2004; Poggianti et al. 2001) to estimate the stellar mass in our sources. The code performs mixed stellar population (MSP) spectrophotometric synthesis. The adopted synthesis stellar population (SSP) library is based on the Padova evolutionary sequences of stellar models (Fagotto et al. 1994a, 1994b) and isochrones (Bertelli et al. 1994), and was computed by assuming a solar metalicity and a Salpeter (1955) initial mass function (IMF) between 0.15 and 120 $M_{\odot}$. The SSP spectra are built using the Pickles (1998) stellar spectral library, and extended to the NIR with the Kurucz (1993) stellar atmosphere models. Nebular features are added based on the ionization code CLOUDY (Ferland 1996). The spectra thus obtained provide a reliable description of simple stellar generations up to $\sim$3 μm in the rest frame. Note that our models do not take fully into account the behavior of AGB stars, in other words they underestimate the contribution from intermediate-age SSPs. We estimate that this results in overestimating stellar masses of at most a factor of 2 (see a discussion in Berta et al. 2007a). Another overestimating factor comes from the assumption of a Salpeter IMF, indeed a Kroupa et al. (1993) or a Chabrier (2003) IMF would yield about 50% lower masses (see Berta et al. 2007a).

The mixed stellar population synthesis combines several phases, adopting a different SFR for each age. This code is well suited for modeling stellar populations of star-forming galaxies, because it allows several, independent episodes of star formation during the life of a galaxy, for example resembling multiple merger-driven starburst events. Age-selective extinction is applied, assuming that the oldest stars have abandoned the dusty medium long ago. Since disk populations are on average affected by a moderate extinction ($A_V \lesssim 1$ mag, e.g., Kennicutt 1998), we adopt a maximum allowed absorption for stars older than 1 Gyr of $A_V = 0.3 - 1.0$ magnitudes. For younger populations the color excess gradually increases, but is limited to $A_V \leqslant 5$. The best fit is sought by means of χ^2 minimization. In the case of nondetections 3σ upper limits are adopted. For each source in the sample, the code explores the SFR extinction parameter space using an Adaptive Simulated Annealing algorithm and records all the attempted models. The uncertainty in the stellar mass estimate is then given by all those solutions whose χ^2 values lie within 3σ from the best fit. Details on the fitting method are described in Berta et al. (2007a).

Assuming that the total energy absorbed in the ultraviolet (UV)–optical domain is processed by dust in the thick molecular clouds embedding young stars and re-emitted in the MIR and FIR (5–1000 μm), we exploit the 24 μm observed flux to constrain the amount of dust and the luminosity of young stellar populations (see Berta et al. 2004, for more details).

The estimated stellar masses and associated uncertainties are listed in Table 7. The stellar masses range from 2.3 to 56 $\times$ 10^{10} $M_{\odot}$, with a median value of 1.8 $\times$ 10^{11} $M_{\odot}$. Although the near-IR SED is dominated by stellar emission, it is possible that an AGN component is also present. Thus these estimates should be considered as upper limits to the true stellar masses. It is also possible that the derived stellar masses overestimate the true masses because our models do not take into account the TP-AGB contribution (Maraston 2005). Indeed such a contribution might yield lower masses, especially at the redshifts of our sources. The stellar masses as a function of redshift are shown in Figure 11. We find that at the same redshift, the stellar masses vary by a factor of 4. No difference in stellar mass is observed between 1.2 mm detected and nondetected objects. Similar masses are observed in objects with a wide range of luminosities and viceversa. For example, all high-z ($z > 1.5$) sources with available spectroscopic redshifts have similar FIR

Table 7
Stellar Masses for the Lockman Hole Sample

Source ID	$M_{\star}$ (10^{11} $M_{\odot}$)	A_V
LH-01	$1.21^{+0.07}_{-0.03}$	$2.32^{+0.02}_{-0.03}$
LH-02	$1.51^{+0.14}_{-0.06}$	$2.27^{+0.05}_{-0.18}$
LH-03	$2.53^{+0.36}_{-0.18}$	$1.70^{+0.06}_{-0.10}$
LH-04	$4.66^{+0.19}_{-0.15}$	$2.51^{+0.03}_{-0.09}$
LH-05	$2.64^{+0.39}_{-0.03}$	$1.85^{+0.02}_{-0.15}$
LH-06	$1.71^{+0.08}_{-0.05}$	$2.37^{+0.04}_{-0.06}$
LH-07	$1.06^{+0.05}_{-0.03}$	$2.30^{+0.03}_{-0.05}$
LH-08	$4.94^{+0.10}_{-0.56}$	$1.67^{+0.02}_{-0.16}$
LH-09	$3.25^{+0.25}_{-0.14}$	$1.80^{+0.04}_{-0.09}$
LH-10	$1.61^{+0.10}_{-0.05}$	$2.13^{+0.05}_{-0.08}$
LH-11	$2.34^{+0.15}_{-0.04}$	$1.93^{+0.03}_{-0.06}$
LH-12	$3.14^{+0.31}_{-0.20}$	$1.25^{+0.03}_{-0.04}$
LH-13	$1.43^{+0.29}_{-0.12}$	$1.76^{+0.02}_{-0.17}$
LH-14	$1.82^{+0.15}_{-0.08}$	$1.85^{+0.04}_{-0.16}$
LH-15	$5.60^{+0.15}_{-0.14}$	$1.86^{+0.05}_{-0.05}$
LH-16	$1.93^{+0.17}_{-0.09}$	$2.73^{+0.03}_{-0.13}$
LH-17	$2.70^{+0.31}_{-0.15}$	$2.05^{+0.04}_{-0.10}$
LH-18	$0.85^{+0.12}_{-0.03}$	$2.85^{+0.02}_{-0.20}$
LH-19	$2.31^{+0.23}_{-0.13}$	$1.74^{+0.20}_{-0.22}$
LH-20	$1.43^{+0.33}_{-0.09}$	$1.79^{+0.16}_{-0.36}$
LH-21	$4.37^{+0.27}_{-0.12}$	$1.88^{+0.05}_{-0.06}$
LH-22	$0.60^{+0.04}_{-0.02}$	$2.49^{+0.08}_{-0.15}$
LH-23	$0.23^{+0.06}_{-0.00}$	$2.82^{+0.02}_{-0.29}$
LH-24	$0.90^{+0.07}_{-0.03}$	$2.43^{+0.03}_{-0.04}$
LH-25	$1.53^{+0.25}_{-0.04}$	$2.17^{+0.02}_{-0.19}$
LH-26	$0.81^{+0.08}_{-0.02}$	$2.76^{+0.03}_{-0.24}$
LH-27	$2.22^{+0.51}_{-0.03}$	$1.42^{+0.02}_{-0.21}$
LH-28	$1.86^{+0.27}_{-0.10}$	$1.76^{+0.05}_{-0.09}$
LH-29	$1.49^{+0.22}_{-0.06}$	$1.98^{+0.16}_{-0.26}$

Note. Uncertainties correspond to 1σ.

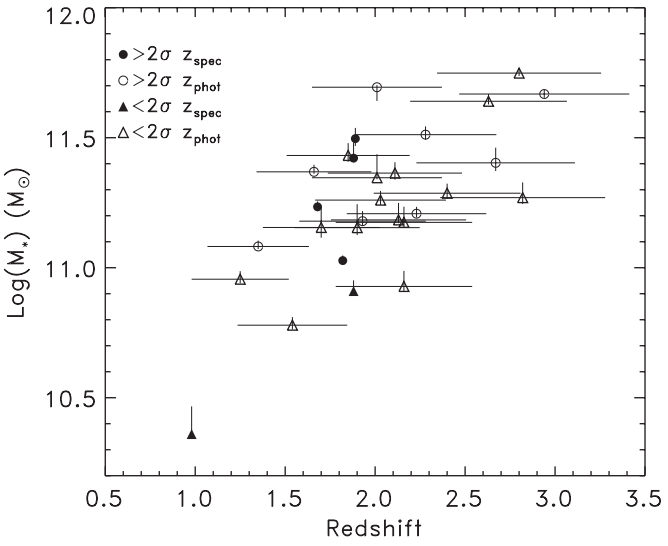

Figure 11. Stellar masses as a function of photometric (open symbols) or spectroscopic (full symbols) redshifts for the SWIRE Lockman Hole sample (29 sources). Circles represent sources with $f_{1.2\,\mathrm{mm}} > 2\sigma$ and triangles represent sources with $f_{1.2\,\mathrm{mm}} < 2\sigma$. Uncertainties on the stellar masses correspond to 2σ.

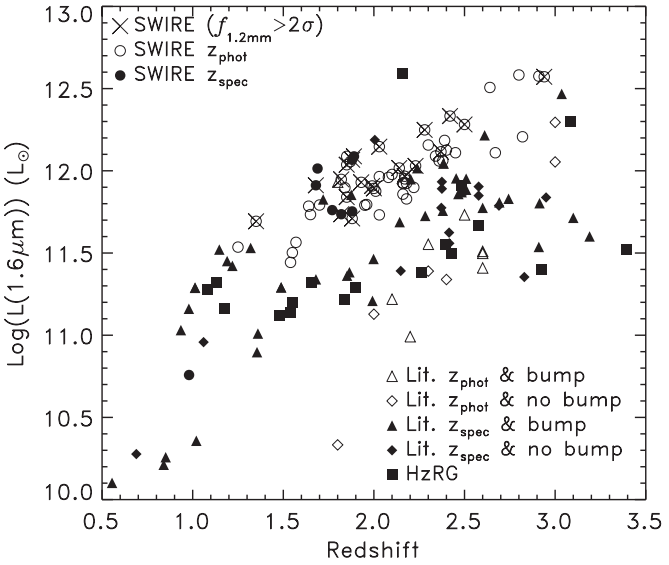

Figure 12. Monochromatic luminosity at 1.6 μm in the rest-frame for SWIRE/MAMBO sources (circles), for literature SMGs (triangles and diamonds), and for high-z radio galaxies (squares). Full symbols represent sources with spectroscopic redshifts and open symbols with photometric redshifts. Triangles represent sources with a typical stellar bump in the IRAC bands and diamonds sources where the bump is not present or not detected. Large crosses are overplotted on SWIRE/MAMBO sources with $f_{1.2\,\mathrm{mm}} > 2\sigma$.

luminosities, $\sim 10^{12.3}\ L_\odot$, but their stellar masses can vary by a factor of 5, i.e., $M_* = 8\text{–}20 \times 10^{10}\ M_\odot$.

8.1. NIR Luminosities

In order to carry out a consistent comparison between the stellar masses of the SWIRE-MAMBO sources with the SMGs found in the literature, we compare their rest-frame luminosity at 1.6 μm, where the stellar emission peaks. The rest-frame luminosity at 1.6 μm is estimated by interpolating the observed IRAC fluxes. The estimated values as a function of redshift are reported in Figure 12. They range from $5.8 \times 10^{10}\ L_\odot$ to $3.8 \times 10^{12}\ L_\odot$, and have a median value of $9.5 \times 10^{11}\ L_\odot$. We compare the luminosities of sources with a spectroscopic redshift and those with only a photometric redshift, and sources with 1.2 mm fluxes greater or lower than 2σ. No apparent difference in NIR luminosity is observed among these subsamples. We also divide the SMGs from the literature in two subgroups (shown as triangles and diamonds in Figure 12), those with a clear stellar bump in the IRAC bands and those for which a bump is not visible because of a different spectral shape or because there are no detections at $\lambda = 5.8$ and 8.0 μm. There is no significant difference in NIR luminosities between the SMGs with and without a stellar bump. The SWIRE-MAMBO sources are systematically more luminous in the NIR, suggesting that they might be more massive than literature SMGs. On average our sources are 3 times more luminous at 1.6 μm than submillimeter selected SMGs. This result is not surprising since our selection is based on a detection at 5.8 μm where the SWIRE 5σ limit is $\simeq$50 μJy, while the literature sample is, on average, characterized by lower 5.8 μm fluxes, and both samples are at similar redshifts.

9. AGN ACTIVITY

It is well established that starburst sources dominate the bulk population of SMGs with only a minor contribution from AGNs. Indeed, although a weak AGN emission is observed in a significant fraction of SMGs, at X-ray energies (Alexander et al. 2005a), in optical spectra lines (Chapman et al. 2005), and in MIR spectra (Valiante et al. 2007; Menéndez-Delmestre et al. 2007; Pope et al. 2008), its contribution to their bolometric luminosity is usually modest ($< 10\%$–20%).

In Section 6.4, the contribution from an obscured AGN to the observed MIR emission of our sources was invoked to explain their unusual colors and SEDs. Based on the available IRS spectra, we estimate, on average, a 34% contribution from a warm dust continuum in the MIR (6–12 μm in the rest frame). Such a component might be generated by an AGN, or by H II regions (Laurent et al. 2000; Dopita et al. 2006). However, this estimate is based on only eight sources. Moreover, the IRS targets include the brightest 24 μm sources of the sample and might thus be biased towards sources with enhanced PAH emission or larger AGN contribution (Brand et al. 2006). To further investigate the presence of an AGN in our sample, we searched for possible signatures using X-ray and radio data.

X-ray observations from *Chandra* of moderate depth (70 ks) are available for 3 LH sources, LH-10, LH-19, and LH-28, from the *Chandra*/SWIRE survey (Polletta et al. 2006), and the CLASX survey (Yang et al. 2004). Although the *XMM* field has a wide shallow (10 ks) X-ray coverage from *XMM-Newton* only one source, *XMM*-03, has been observed by *XMM-Newton* (Pierre et al. 2007), and it is at the edge of the field. Out of four sources with X-ray coverage, only LH-10 is detected in the X-ray. The X-ray 0.4–8 keV flux of LH-10 is 2.1×10^{-15} ergs cm^{-2} s^{-1}, and the hardness ratio is HR $= -0.7$ (Yang et al. 2004), as expected for a steep unabsorbed power-law spectrum. The estimated 0.4–8 keV luminosity is 5.7×10^{43} ergs s^{-1}, consistent with being AGN powered and with those measured in X-ray detected SMGs in HDFN (Alexander et al. 2005b). Although, based on the hardness ratio, the X-ray spectrum appears unabsorbed, the derived $L_{\mathrm{MIR}}/L_{\mathrm{X-ray}}$ ratio, $\simeq$100, is much higher than commonly observed in AGNs, 0.3–10, (see e.g., Franceschini et al. 2005; Polletta et al. 2007). The large $L_{\mathrm{MIR}}/L_{\mathrm{X-ray}}$ ratio suggests that the X-ray luminosity is underestimated and that the observed X-ray emission corresponds to a small fraction of the intrinsic X-ray emission, perhaps due to a

reflected component (warm scattering), while the intrinsic X-ray emission is completely absorbed. The lack of X-ray detections of the other 3 sources does not rule out the presence of an absorbed X-ray luminous AGN ($L_{\rm X-ray} > 10^{44}$ ergs s^{-1}) or an unabsorbed AGN of moderate luminosity ($L_{\rm X-ray} < 10^{44}$ ergs s^{-1}). Indeed the detection limit of the *Chandra* observations corresponds to X-ray luminosities $\geqslant 10^{44}$ ergs s^{-1} for an unabsorbed AGN at the redshift of our sources. An AGN of lower luminosity or absorbed, as typically found in SMGs, would not be detected at our depths.

Deep VLA radio observations at 20 cm are available in a 0.4 deg^2 area centered on the *Chandra*/SWIRE field (Polletta et al. 2006, Owen & Morrison 2008) in the LH, and shallow radio observations are available from the VLA FIRST survey in all fields[20] (Condon et al. 1998). LH-11, and LH-22 are the only sources that fall in the deep VLA field and are both detected, with 20 cm fluxes of 82 and 51 μJy, respectively. A third source, LH-28, is detected by the FIRST survey. The radio fluxes are reported in Table 1. The radio source associated with LH-28 is extended, $6\farcs66 \times 3\farcs16$, corresponding to 57 kpc $\times$ 27 kpc. The bright radio flux and radio extension, combined with the lack of mm detection, indicate that the radio emission of LH-28 is powered by a jet and it is, thus, an AGN. LH-11, and LH-22 are not resolved in the radio images, $< 1\farcs24$ and $0\farcs87$, respectively. Although their 1.4 GHz rest-frame radio luminosities are large, respectively, $10^{28.2}$ and $10^{27.8}$ W Hz^{-1}, they are not in excess of what is expected based on the FIR-radio relationship found in both starburst and radio-quiet AGNs (Condon et al. 1998). Therefore, the available radio data do not imply or rule out the presence of an AGN in these two luminous radio sources.

In summary, the available X-ray and radio data indicate that at least one out of three sources contains an AGN. This fraction is consistent with that derived from IRS spectroscopy ($\geqslant 30\%$), but all these samples are limited by small number statistics and there is no overlap among them, leaving the question on the AGN contribution and role in our SWIRE-MAMBO sample unanswered. Moreover, the subset of sources observed with the IRS might be biased towards a certain type of sources, for example with enhanced PAHs, and might not be representative of the whole SWIRE-MAMBO sample. Yet, since there is no apparent difference in the 1.2 mm/24 μm flux ratios of the X-ray and radio AGNs and the IRS sample, the estimated AGN contribution might be valid for the whole SWIRE-MAMBO sample. However, altough it is quite likely that an AGN is present in a large fraction of our sources, it is not expected to significantly contribute to their MIR emission, as is also the case for the classical SMGs (see e.g., Pope et al. 2008). Indeed, even by taking this contribution into account, we still find smaller $f_{1.2\,\mu{\rm m}}/f_{24\,\mu{\rm m}}$ flux ratios, larger FIR luminosities, and a FIR peak at shorter wavelengths than in classical SMGs. Thus, as already stated in Section 6.4, it is unlikely that the difference between the SWIRE-MAMBO sources and classical SMGs is due to a more important AGN contribution in our sample.

10. DISCUSSION

In the previous sections we have investigated the multiwavelength properties of the SWIRE-MAMBO sources selected here and compared them with those of classical SMGs. Our sources are characterized by redshifts, $1< z <3$, and millimeter fluxes in the same range as classical SMGs. Compared to classical SMGs, they are in general brighter at mid and near infrared wavelengths. Their FIR luminosities, constrained for the sources detected at 1.2 mm, are in the ULIRG range, $\geqslant 10^{12}$ $L_\odot$. Their FIR emission is likely dominated by warmer dust than estimated in classical SMGs, but this result needs to be confirmed by additional submillimeter data. Their stellar masses are large, $10^{10.3}$ to $10^{11.8}$ $M_\odot$, and their NIR luminosities and, likely stellar masses, are also higher by about a factor of 3 than in classical SMGs. Although some of these estimates are characterized by large uncertainties, it is a clear that our sources do show some differences compared to classical SMGs, or that they belong to a subclass of SMGs with larger MIR/FIR flux ratios than the bulk of SMGs (Figure 8). Indeed, SMGs with a relatively small 1.2 mm/24 μm flux ratio represent only a minority of all SMGs reported in the literature.

The possible origin of the observed differences between our sources and classical SMGs are discussed here. Warm dust emission is an indicator of strong overall heating of the dust. A large infrared luminosity and faint optical/UV emission implies elevated dust opacity, which in turn might imply a larger density of interstellar dust closer to the heating sources, or a more efficient heating mechanism relative to the dust (Dale et al. 2007; Kovács et al. 2006). Dust heating is predominantly fueled by the emission from massive (> 8 $M_\odot$) stars in star-forming regions (Kovács et al. 2006), or by an AGN radiation field. The peak of IR emission of cold dust can thus shift towards shorter wavelengths if (1) the radiation field is higher because of younger stellar populations (Piovan et al. 2006), or (2) a significant contribution from AGN-heated dust is present. Thus, the difference in the FIR emission peak between our sample and classical SMGs (see Section 7) might be an indication of more massive stars relative to dust mass, or of a more significant AGN contribution in our SWIRE-MAMBO sources compared to classical SMGs.

The latter scenario has been investigated by measuring the intensity and equivalent width of the PAH features; weak PAH emission is indicative of an important AGN contribution. Since the average MIR spectrum, and thus the PAH equivalent width, of our sources and of classical SMGs are consistent (see Figure 9), a significant AGN contribution is disfavored. This result supports the alternative scenario of a higher contribution of massive stars relative to the dust mass. However, the available data do not allow us to test this hypothesis and rule out other explanations, perhaps related to the star forming region geometry and distribution (see e.g., Farrah et al. 2008).

Our results indicate that our selection has revealed a class of ULIRGs that is underrepresented in current SMG samples. The SWIRE-MAMBO sources indeed cover a different region in the luminosity-temperature ($L - T_d$) diagram than classical SMGs and bridge the gap between the latter and local ULIRGs (see Chapman et al. 2003; Lewis et al. 2005). Similar results have been obtained by a study of a similar sample of *Spitzer*-selected sources with known spectroscopic redshifts from strong PAH features, and multiple FIR detections (Younger et al. 2008).

11. SUMMARY AND CONCLUSION

Using the SWIRE survey and the MAMBO camera on the IRAM 30m telescope, we have identified 21 ULIRGs at $z \simeq 1$–3 with average 1.2 mm fluxes of 2.9 ± 0.2 mJy. They are characterized by starburst-dominated SEDs and by unusually large MIR/FIR flux ratios. These sources were discovered among a sample of 61 ULIRG $z > 1$ candidates selected

[20] The VLA FIRST source catalog and images are available from http://sundog.stsci.edu.

in the SWIRE survey that were followed-up with MAMBO observations at 1.2 mm.

The primary selection criteria of the SWIRE sample of ULIRG candidates are a peak in the IRAC 5.8 μm band due to the red-shifted near-infrared spectrum of evolved stars, a bright (>400 μJy) detection at 24 μm, and a faint optical counterpart ($r' > 23$). The average 1.2 mm flux of the whole sample is 1.5 $\pm$ 0.2 mJy.

The optical–MIR SEDs of the selected sources are consistent with those of starburst galaxies. Photometric redshifts are estimated by fitting the SEDs with galaxy templates. For eight sources, spectroscopic redshifts from MIR spectra obtained with IRS on board of *Spitzer* are available and are in reasonable agreement with the estimated photometric redshifts.

Our analysis focuses on 29 sources in the Lockman Hole field where the average 1.2 mm flux (1.9 $\pm$ 0.3 mJy) is higher than in the *XMM*-LSS, ELAIS-N1 & ELAIS-N2 fields (1.1 $\pm$ 0.2 mJy). However, we also present basic results for 32 sources from the other fields, which were less thoroughly observed. The fraction of LH sources with 1.2 mm fluxes $\geqslant 2\sigma$ is $\sim$40% (24% at 4σ; see Table 3). This fraction is much higher than previously found for *Spitzer* MIR selected samples (23%, 18%, and 10% at $\geqslant 2, 3$, and 4σ, respectively; Lutz et al. 2005). We attribute this difference to the fact that earlier samples favored AGN-dominated, rather than starburst-dominated systems. Our sample, on the other hand, shows systematically lower 1.2 mm/24 μm flux ratios than the majority of *Spitzer*-detected submillimeter-selected SMGs. Such a difference is attributed to a bias in our selection in favor of 24 μm-bright systems compared to the selection of SMGs.

Far-infrared luminosities are estimated assuming a z-dependent dust temperature as observed in classical SMGs, and normalizing a greybody model to the observed mm flux. Average 70 and 160 μm fluxes from stacked *Spitzer*/MIPS images are measured. The mean FIR stacked fluxes are $\sim$4 times larger than the fluxes predicted by the greybody models, suggesting higher FIR luminosities and a FIR peak at shorter wavelengths than in classical SMGs. The SWIRE-MAMBO sources are ULIRGs in the $z = 1.5$–3 range with FIR luminosities from 10^{12} to $10^{13.3}$ $L_{\odot}$. Stellar masses, estimated by modeling the optical–infrared data with stellar synthesis populations, are also large, $\sim (0.2\text{–}6) \times 10^{11}$ $M_{\odot}$, suggesting that these systems might be the precursors of the most massive ellipticals.

Compared to submillimeter selected galaxies (SMGs), the SWIRE-MAMBO sources are among those with the largest 24 μm mm^{-1} flux ratios. The origin of such large ratios is investigated by comparing the average mid-infrared spectra and the stacked far-infrared spectral energy distributions of our sources and classical SMGs.

The mid-infrared spectra, available for a handful of sources, show strong PAH features and a warm dust continuum. The warm dust continuum contributes $\sim$34% of the mid-infrared emission, and is likely associated with an AGN component. This constribution is consistent with what is found in SMGs, and indeed the PAH equivalent widths are, on average, similar in our sources and in SMGs. Thus, even taking into account the AGN component, the 24 μm/1.2 mm flux ratios remain larger than typically observed in SMGs. The hypothesis of contribution from AGN emission to the MIR is thus disfavored, and it is more likely that the large ratios are due to more luminous PAH emission than in classical SMGs.

The analysis of the stacked far-infrared SEDs yields warmer dust temperatures than typically observed in classical SMGs. Thus, our selection has favored a warm class of ultraluminous infrared sources at high-z that is rarely found in current SMG samples. Indeed classical SMGs are not common among bright 24 μm sources such as the SWIRE-MAMBO sample (e.g., only about 20% of SMGs have $f_{24\,\mu\mathrm{m}} > 0.4$ mJy). Our sample occupies a region in the $L - T_d$ diagram that is underpopulated by classical SMGs, implying that ULIRGs at high-z might exhibit a similar range in dust temperatures as local ULIRGs (see Chapman et al. 2003; Lewis et al. 2005). The analysis of our sample suggests that warmer ULIRGs are brighter MIR sources due to exhibiting more luminous PAH emission than cooler ULIRGs. However, to confirm such a correlation, an analysis of the MIR spectra for a larger sample of 24 μm-selected objects with known mm fluxes would be necessary. This analysis will be soon possible with other *Spitzer* samples that have been or will be observed with the IRS and with MAMBO (Younger et al. 2008, G. Lagache et al. 2009, in preparation).

Our sample is the largest *Spitzer*-selected sample detected at millimeter wavelengths currently available.

We thank the referee for useful comments that improved the paper. C.J.L. and M.P. thank Bruce Elmegreen and Jakob Walcher for helpful discussion. We are grateful to Elisabetta Valiante for providing the average IRS spectrum of a sample of SMGs. M.P. acknowledges financial support from the Marie-Curie Fellowship grant MEIF-CT-2007-042111. This work is based on observations made with the IRAM 30m Telescope and the *Spitzer Space Telescope*. The IRAM 30m Telescope is funded by the Centre National de la Recherche Scientifique (France), the Max-Planck Gesellschaft (Germany), and the Instituto Geografico Nacional (Spain). The *Spitzer Space Telescope* is operated by the Jet Propulsion Laboratory, California Institute of Technology under NASA contract 1407. Support for this work, part of the *Spitzer Space Telescope* Legacy Science Program, was provided by NASA through an award issued by the Jet Propulsion Laboratory, California Institute of Technology under NASA contract 1407. We thank the IRAM staff for their support during the observations, and E. Kreysa and his group for providing the MAMBO bolometer array. This research has made use of the NASA/IPAC Extragalactic Database (NED) which is operated by the Jet Propulsion Laboratory, California Institute of Technology, under contract with the National Aeronautics and Space Administration.

Facilities: Spitzer (IRAC,MIPS), IRAM(MAMBO).

APPENDIX

SED FITS AND PHOTOMETRIC REDSHIFTS

The best and acceptable fits to the optical ($Ugriz$) and MIR (3.6–24 μm) SEDs of each source, obtained as described in Section 5 are shown in Figure 13. We report a maximum of three solutions, those with the lowest 3 χ^2. In case a spectroscopic redshift is available, the best-fit template at the spectroscopic redshift is reported as dotted curve. Although the templates extend to FIR wavelengths, the FIR data are not used in the fitting procedure and in the χ^2 computation. The parameters (template, and redshift) of each solution are reported in Table 4.

Eight sources have spectroscopic redshifts and are shown in Figures 13(a), (c), and (f). It can be appreciated from this figure that with only the broad NIR bump to constrain the photometric redshift, using the broad IRAC filters, a redshift accuracy of 10% in (1+z) is a reasonable expectation. In some cases, a NIR bump can be present in sources at lower redshift. Indeed the presence of warm dust continuum can make the NIR bump or the turnover

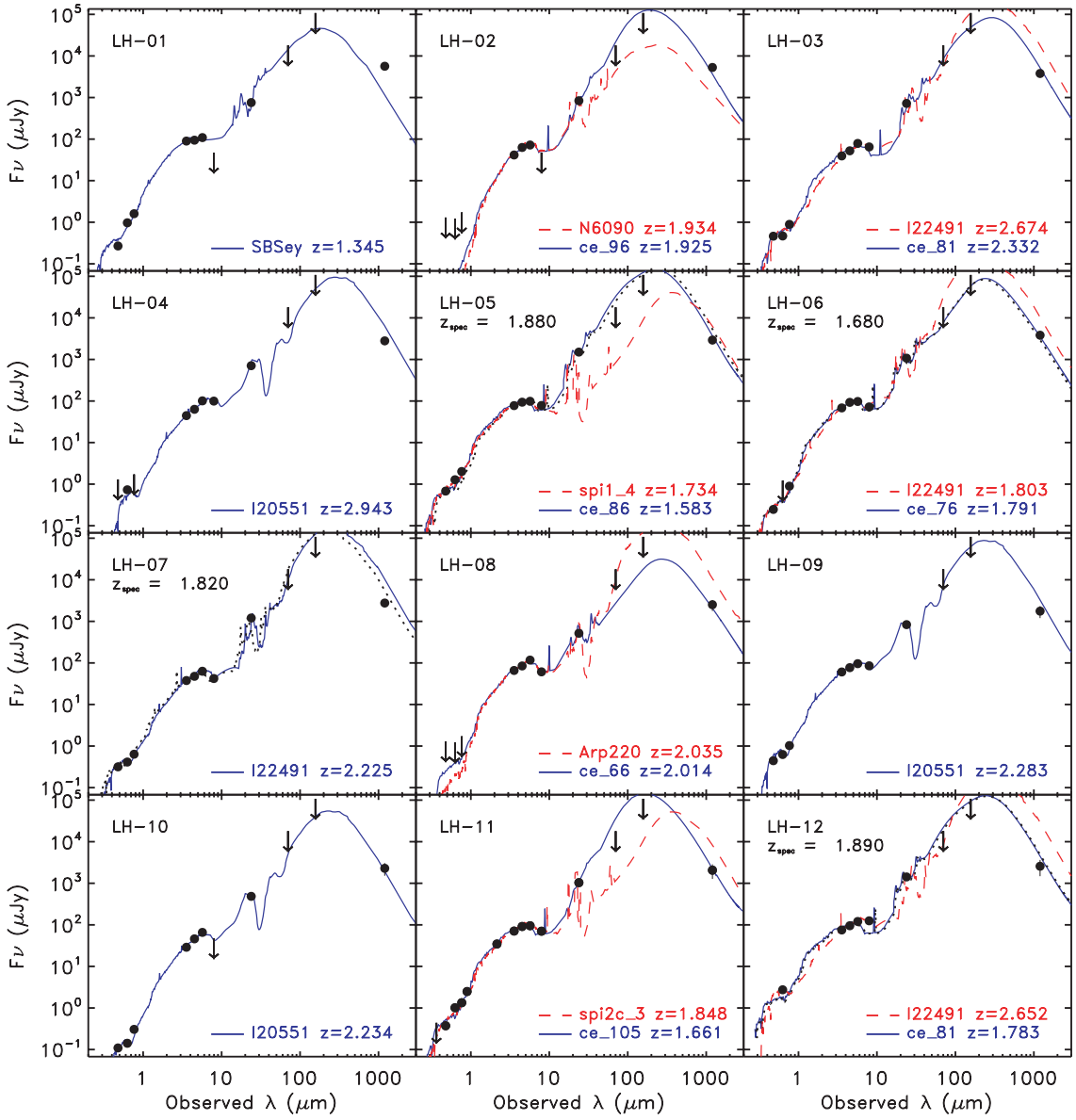

(a)

Figure 13. *a)* Optical-IR SEDs of MAMBO sources in the Lockman Hole field (*a, b, c*), in the ELAIS-N1 field (*d, e*), in the ELAIS-N2 field (*f*), and in the *XMM*-LSS field (*g*). The solid curves represent different fits to the optical–MIR data (up to 24 μm). Solid blue, dashed red, and dotted green curves corrrespond to fits with increasing χ^2. The template name and photometric redshift of each fit are annotated. The dotted black curve corresponds to the best-fit template plotted at the spectroscopic redshifts. The source ID number, and the spectroscopic redshift when available, are reported on the upper left corner in each panel. Downward arrows represent 5σ upper limits at optical and infrared wavelengths, and 3σ upper limits at 1.2 mm.

(An extended version of this figure and the color version of Figure 13a are available in the online journal.)

at 8 μm less pronounced and even shift the stellar peak to longer wavelengths (Berta et al. 2007b; Daddi et al. 2007). Also strong emission from the 3.3 μm PAH feature falling into the 5.8 μm filter can produce a peak in the IRAC SED that would be wrongly interpreted if no optical or NIR data were available. These two effects increase the uncertainty associated with the photometric redshift estimate. Some examples can be seen in the fit to source LH-12 ($z_{\rm spec} = 1.89$ and $z_{\rm phot} = 2.65$) and LH-23 ($z_{\rm spec} = 0.98$ and $z_{\rm phot} = 1.21$) in Figures 13(a) and (c).

REFERENCES

Alexander, D. M., Bauer, F. E., Chapman, S. C., Smail, I., Blain, A. W., Brandt, W. N., & Ivison, R. J. 2005a, ApJ, 632, 736

Alexander, D. M., Bauer, F. E., Chapman, S. C., Smail, I., Blain, A. W., Brandt, W. N., & Ivison, R. J. 2005b, ApJ, 632, 736

Ashby, M. L. N., et al. 2006, ApJ, 644, 778

Berta, S. 2005, PhD thesis, Univ. Padua

Berta, S., Fritz, J., Franceschini, A., Bressan, A., & Lonsdale, C. 2004, A&A, 418, 913

Berta, S., Fritz, J., Franceschini, A., Bressan, A., & Pernechele, C. 2003, A&A, 403, 119

Berta, S., et al. 2007a, A&A, 476, 151

Berta, S., et al. 2007b, A&A, 467, 565

Bertelli, G., Bressan, A., Chiosi, C., Fagotto, F., & Nasi, E. 1994, A&AS, 106, 275

Blakeslee, J. P., Davis, M., Tonry, J. L., Dressler, A., & Ajhar, E. A. 1999, ApJ, 527, L73

Bolzonella, M., Miralles, J.-M., & Pelló, R. 2000, A&A, 363, 476

Borys, C., Chapman, S., Halpern, M., & Scott, D. 2003, MNRAS, 344, 385

Borys, C., Smail, I., Chapman, S. C., Blain, A. W., Alexander, D. M., & Ivison, R. J. 2005, ApJ, 635, 853
Brand, K., et al. 2006, ApJ, 644, 143
Calzetti, D., Armus, L., Bohlin, R. C., Kinney, A. L., Koornneef, J., & Storchi-Bergmann, T. 2000, ApJ, 533, 682
Chabrier, G. 2003, PASP, 115, 763
Chapman, S. C., Blain, A. W., Smail, I., & Ivison, R. J. 2005, ApJ, 622, 772
Chapman, S. C., Helou, G., Lewis, G. F., & Dale, D. A. 2003, ApJ, 588, 186
Chapman, S. C., Smail, I., Blain, A. W., & Ivison, R. J. 2004, ApJ, 614, 671
Charmandaris, V., et al. 2004, ApJS, 154, 142
Chary, R., & Elbaz, D. 2001, ApJ, 556, 562
Clavel, J., et al. 2000, A&A, 357, 839
Clements, D. L., et al. 2008, MNRAS, 387, 247
Condon, J. J., Cotton, W. D., Greisen, E. W., Yin, Q. F., Perley, R. A., Taylor, G. B., & Broderick, J. J. 1998, AJ, 115, 1693
Coppin, K., et al. 2006, MNRAS, 372, 1621
Daddi, E., et al. 2007, ApJ, 670, 173
Dale, D. A., et al. 2007, ApJ, 655, 863
Desai, V., et al. 2008, ApJ, 669, 810
Dey, A., et al. 2008, ApJ, 677, 943
Dole, H., et al. 2006, A&A, 451, 417
Dopita, M. A., et al. 2006, ApJ, 639, 788
Dunlop, J., Peacock, J., Spinrad, H., Dey, A., Jimenez, R., Stern, D., & Windhorst, R. 1996, Nature, 381, 581
Efron, B., & Tibshirani, R. 1993, in An Introduction to the Bootstrap (Ney York: Chapman and Hall)
Egami, E., et al. 2004, ApJS, 154, 130
Elvis, M., et al. 1994, ApJS, 95, 1
Fagotto, F., Bressan, A., Bertelli, G., & Chiosi, C. 1994a, A&AS, 104, 365
Fagotto, F., Bressan, A., Bertelli, G., & Chiosi, C. 1994b, A&AS, 105, 29
Farrah, D., et al. 2008, ApJ, 677, 957
Fazio, G. G., et al. 2004, ApJS, 154, 10
Ferland, G. J. 1996, Hazy, A Brief Introduction to Cloudy 90 (University of Kentucky Internal Report)
Franceschini, A., et al. 2005, AJ, 129, 2074
Frayer, D. T., et al. 2004a, ApJS, 154, 137
Frayer, D. T., et al. 2006, AJ, 131, 250
Frayer, D. T., Reddy, N. A., Armus, L., Blain, A. W., Scoville, N. Z., & Smail, I. 2004b, AJ, 127, 728
Greve, T. R., et al. 2005, MNRAS, 359, 1165
Greve, T. R., Ivison, R. J., Bertoldi, F., Stevens, J. A., Dunlop, J. S., Lutz, D., & Carilli, C. L. 2004, MNRAS, 354, 779
Helou, G., Khan, I. R., Malek, L., & Boehmer, L. 1988, ApJS, 68, 151
Houck, J. R., et al. 2004, ApJS, 154, 18
Houck, J. R., et al. 2005, ApJ, 622, L105
Hughes, D. H., et al. 1998, Nature, 394, 241
Huynh, M. T., Pope, A., Frayer, D. T., & Scott, D. 2007, ApJ, 659, 305
Ivison, R. J., et al. 2007, MNRAS, 380, 199
Ivison, R. J., et al. 2004, ApJS, 154, 124
Kennicutt, R. C., Jr. 1998, ApJ, 498, 541
Kovács, A., Chapman, S. C., Dowell, C. D., Blain, A. W., Ivison, R. J., Smail, I., & Phillips, T. G. 2006, ApJ, 650, 592
Kreysa, E., et al. 1998, in Proc. SPIE 3357, 319
Kroupa, P., Tout, C. A., & Gilmore, G. 1993, MNRAS, 262, 545
Kurucz, R. 1993, ATLAS9 Stellar Atmosphere Programs and 2 km/s grid. Kurucz CD-ROM No. 13 (Cambridge, MA.: Smithsonian Astrophysical Observatory)
Laurent, O., Mirabel, I. F., Charmandaris, V., Gallais, P., Madden, S. C., Sauvage, M., Vigroux, L., & Cesarsky, C. 2000, A&A, 359, 887
Lewis, G. F., Chapman, S. C., & Helou, G. 2005, ApJ, 621, 32
Lonsdale, C. J., Farrah, D., & Smith, H. E. 2006, in Astrophysics Update 2, ed. J. W. Mason (Heidelberg: Springer), 285
Lonsdale, C. J., et al. 2003, PASP, 115, 897
Lutz, D., Yan, L., Armus, L., Helou, G., Tacconi, L. J., Genzel, R., & Baker, A. J. 2005, ApJ, 632, L13
Maraston, C. 2005, MNRAS, 362, 799
Menéndez-Delmestre, K., et al. 2007, ApJ, 655, L65
Mortier, A. M. J., et al. 2005, MNRAS, 363, 563
Owen, F. N., & Morrison, G. E. 2008, AJ, 136, 1889
Pickles, A. J. 1998, PASP, 110, 863
Pierre, M., et al. 2007, MNRAS, 382, 279
Piovan, L., Tantalo, R., & Chiosi, C. 2006, MNRAS, 366, 923
Poggianti, B. M., Bressan, A., & Franceschini, A. 2001, ApJ, 550, 195
Polletta, M., et al. 2006, ApJ, 642, 673
Polletta, M., et al. 2007, ApJ, 663, 81
Polletta, M., et al. 2008, A&A., 492, 81
Pope, A., Borys, C., Scott, D., Conselice, C., Dickinson, M., & Mobasher, B. 2005, MNRAS, 358, 149
Pope, A., et al. 2008, ApJ, 675, 1171
Pope, A., et al. 2006, MNRAS, 370, 1185
Rieke, G. H., et al. 2004, ApJS, 154, 25
Sajina, A., Yan, L., Armus, L., Choi, P., Fadda, D., Helou, G., & Spoon, H. 2007, ApJ, 664, 713
Salpeter, E. E. 1955, ApJ, 121, 161
Sanders, D. B., & Mirabel, I. F. 1996, ARA&A, 34, 749
Sanders, D. B., Soifer, B. T., Elias, J. H., Neugebauer, G., & Matthews, K. 1988, ApJ, 328, L35
Sawicki, M. 2002, AJ, 124, 3050
Scott, S. E., et al. 2002, MNRAS, 331, 817
Seymour, N., et al. 2007, ApJS, 171, 353
Silva, L., Granato, G. L., Bressan, A., & Danese, L. 1998, ApJ, 509, 103
Simpson, C., & Eisenhardt, P. 1999, PASP, 111, 691
Smail, I., Chapman, S. C., Blain, A. W., & Ivison, R. J. 2004, ApJ, 616, 71
Spergel, D. N., et al. 2003, ApJS, 148, 175
Surace, J. A., et al. 2005, The SWIRE Data Release 2: Image Atlases and Source Catalogs for ELAIS-N1, ELAIS-N2, *XMM*-LSS, and the Lockman Hole, Data Delivery Document (*Spitzer Science Center*, California Institute of Technology, Pasadena, CA) http://swire.ipac.caltech.edu/swire/astronomers/publications/SWIRE_doc_083105.pdf
Tacconi, L. J., et al. 2006, ApJ, 640, 228
Valiante, E., Lutz, D., Sturm, E., Genzel, R., Tacconi, L. J., Lehnert, M. D., & Baker, A. J. 2007, ApJ, 660, 1060
Voss, H., Bertoldi, F., Carilli, C., Owen, F. N., Lutz, D., Holdaway, M., Ledlow, M., & Menten, K. M. 2006, A&A, 448, 823
Weedman, D., et al. 2006, ApJ, 653, 101
Weedman, D. W., et al. 2005, ApJ, 633, 706
Yan, L., et al. 2005, ApJ, 628, 604
Yan, L., et al. 2007, ApJ, 658, 778
Yang, Y., Mushotzky, R. F., Steffen, A. T., Barger, A. J., & Cowie, L. L. 2004, AJ, 128, 1501
Younger, J. D., et al. 2008, MNRAS, in press (arXiv:0812.2476)
Yun, M. S., et al. 2008, arXiv e-prints, 806